https://doi.org/10.1093/nar/gkad121

NAR Breakthrough Article

Dynamic interplay between RPL3- and RPL3L-containing ribosomes modulates mitochondrial activity in the mammalian heart

Ivan Milenkovic[1,2], Helaine Graziele Santos Vieira[1], Morghan C. Lucas[1,2], Jorge Ruiz-Orera[3], Giannino Patone[3], Scott Kesteven[4], Jianxin Wu[4], Michael Feneley[4], Guadalupe Espadas[1,2], Eduard Sabidó[1,2], Norbert Hübner[3,5,6], Sebastiaan van Heesch[7], Mirko Völkers[8] and Eva Maria Novoa[1,2,*]

[1]Centre for Genomic Regulation (CRG), The Barcelona Institute of Science and Technology, Dr. Aiguader 88, Barcelona 08003, Spain, [2]Universitat Pompeu Fabra (UPF), Barcelona, Spain, [3]Cardiovascular and Metabolic Sciences, Max Delbrück Center for Molecular Medicine in the Helmholtz Association (MDC), D-13125 Berlin, Germany, [4]Victor Chang Cardiac Research Institute, Darlinghurst, NSW 2010, Australia, [5]Charité -Universitätsmedizin, D-10117 Berlin, Germany, [6]German Centre for Cardiovascular Research (DZHK), Partner Site Berlin, D-13347 Berlin, Germany, [7]Princess Máxima Center for Pediatric Oncology, Heidelberglaan 25, 3584 CS, Utrecht, The Netherlands and [8]University of Heidelberg, Heidelberg, Germany

Received November 23, 2022; Revised January 31, 2023; Editorial Decision February 02, 2023; Accepted February 09, 2023

ABSTRACT

The existence of naturally occurring ribosome heterogeneity is now a well-acknowledged phenomenon. However, whether this heterogeneity leads to functionally diverse 'specialized ribosomes' is still a controversial topic. Here, we explore the biological function of RPL3L (uL3L), a ribosomal protein (RP) paralogue of RPL3 (uL3) that is exclusively expressed in skeletal muscle and heart tissues, by generating a viable homozygous *Rpl3l* knockout mouse strain. We identify a rescue mechanism in which, upon RPL3L depletion, RPL3 becomes upregulated, yielding RPL3-containing ribosomes instead of RPL3L-containing ribosomes that are typically found in cardiomyocytes. Using both ribosome profiling (Ribo-seq) and a novel orthogonal approach consisting of ribosome pulldown coupled to nanopore sequencing (Nano-TRAP), we find that RPL3L modulates neither translational efficiency nor ribosome affinity towards a specific subset of transcripts. In contrast, we show that depletion of RPL3L leads to increased ribosome–mitochondria interactions in cardiomyocytes, which is accompanied by a significant increase in ATP levels, potentially as a result of fine-tuning of mitochondrial activity. Our results demonstrate that the existence of tissue-specific RP paralogues does not necessarily lead to enhanced translation of specific transcripts or modulation of translational output. Instead, we reveal a complex cellular scenario in which RPL3L modulates the expression of RPL3, which in turn affects ribosomal subcellular localization and, ultimately, mitochondrial activity.

GRAPHICAL ABSTRACT

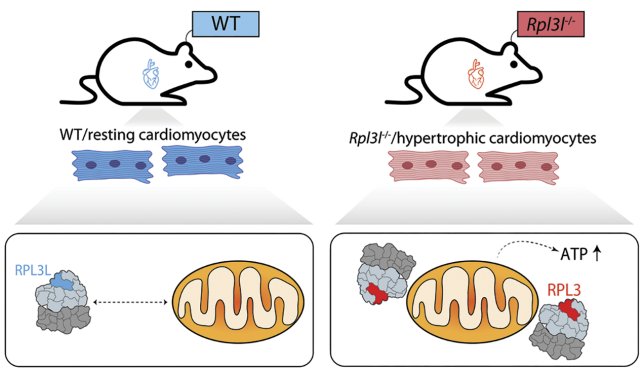

*To whom correspondence should be addressed. Tel: +34 93 316 0131; Email: eva.novoa@crg.eu

INTRODUCTION

A major challenge in biology is to comprehend how protein synthesis is regulated with high precision, in both the spatial and the temporal context. While many layers of gene expression regulation have been extensively studied over the years, ribosomes have been historically perceived as static and passive elements that do not partake in regulatory processes. Several works, however, have challenged this view (1–6), and have provided evidence that ribosomes with specialized functions exist, and can preferentially translate specific subsets of mRNAs (7). While naturally occurring ribosome heterogeneity is now a well-documented phenomenon (8–10), whether this heterogeneity leads to functionally diverse 'specialized ribosomes' is still a controversial topic (11–14).

Ribosomes are supramolecular ribonucleoprotein complexes responsible for protein synthesis in all known organisms. Eukaryotic ribosomes consist of two subunits: the small 40S subunit, which is typically made up of 32 ribosomal proteins (RPs) and the 18S rRNA, and the large 60S subunit, typically comprised of 47 RPs and the 5S, 5.8S and 28S rRNAs (15). While the structure and composition of ribosomes were thought to be largely invariant (16), several studies that examined the dynamics of RP composition and their relationship with ribosome function suggest the contrary (2,7,9,11,17–20). For example, RP stoichiometry in yeast and mouse stem cells was shown to depend on the number of ribosomes bound per mRNA (9). Similarly, RPL38 was shown to be of paramount importance for the translation of Homeobox mRNAs in mice (2), while RPL10A-containing ribosomes were found to preferentially translate a subpool of mRNAs in mouse stem cells (7).

Many species contain many duplicated genes encoding RPs, which for a long time were thought to be functionally redundant (21,22). However, a pioneering study in yeast revealed that depletion of RP paralogues does not lead to the same phenotypes, suggesting paralogue-specific functions (3). In mammals, RP paralogues have been shown to be differentially expressed upon tumorigenesis (10) and some of them are exclusively expressed in restricted subsets of tissues (8,10). For example, *Rpl3* is constitutively expressed in all tissues, whereas the expression of its paralogue gene, *Rpl3l*, is restricted to heart and skeletal muscle tissues (23). Thus, while the existence of heterogeneous ribosomes in terms of RP composition is well documented (24,25), the biological function of RP paralogue genes with restricted tissue-specific expression, such as *Rpl3l*, is largely unknown.

The human *Rpl3l* gene was first identified in studies focusing on autosomal dominant polycystic kidney disease gene regions, in which the authors identified a gene sharing 77% identity at the protein level with the consensus mammalian *Rpl3* gene (26,27). These studies found that RPL3L was exclusively expressed in heart and skeletal muscle, but no further indications were found as to its role in these tissues (27). Two decades later, it was found that RPL3L (uL3L) is down-regulated upon hypertrophic stimuli, and it was proposed that RPL3L (uL3L) may function as a negative regulator of muscle growth (15). In support of this hypothesis, mutations in the human *Rpl3l* gene have been linked to several heart disorders, including atrial fibrillation (28,29) and childhood-onset cardiomyopathy (30). However, why certain tissues express distinct RPs, and with what biological relevance, still remains unclear.

Here, we used a combination of wet lab and bioinformatics techniques to study the role of the RPL3 (uL3)–RPL3L (uL3L) pair in protein translation in the mouse heart. We found that *Rpl3l* is expressed only post-natally, with its expression limited to specific cell types, in addition to being restricted to heart and muscle tissues. Specifically, we observed that in hearts, *Rpl3l* was exclusively expressed in cardiomyocytes, whereas *Rpl3* was mainly expressed in non-myocyte heart cell types. To explore the biological function of *Rpl3l*, we generated a viable homozygous *Rpl3l*$^{-/-}$ mouse strain, and identified a rescue mechanism in which RPL3 becomes up-regulated upon *Rpl3l* knockout, yielding RPL3-containing ribosomes instead of RPL3L-containing ribosomes that are typically found in mouse cardiomyocytes. Using both ribosome profiling (Ribo-seq) and ribosome pulldown coupled to nanopore sequencing (Nano-TRAP), we identified only a handful of differentially translated transcripts in *Rpl3l*$^{-/-}$ hearts, suggesting that RPL3L does not play a major role in modulating translation efficiency or ribosome affinity towards preferentially translating a specific subset of transcripts. In contrast, when coupling ribosome pulldown to proteomics (Proteo-TRAP), we found that a very large amount of mitochondrial proteins were significantly enriched in RPL3-containing ribosome immunoprecipitates in cardiomyocytes. We then confirmed that RPL3, unlike RPL3L, is detected in the mitochondrial fraction of heart lysates, suggesting that the use of either of the two paralogues might be fine-tuning the ribosome–mitochondria interactions in cardiomyocytes. Moreover, we show that ATP levels, but not mitochondrial abundance, are significantly increased in *Rpl3l*$^{-/-}$ cardiomyocytes.

Altogether, our work reveals that upon depletion of *Rpl3l*, RPL3 is up-regulated, mimicking the RPL3/RPL3L interplay that occurs upon hypertrophic stimuli (15). This switch in RPL3/RPL3L expression patterns causes RPL3 to replace RPL3L in cardiac or skeletal muscle ribosomes, which in turn leads to a higher proportion of ribosome-bound mitochondria and consequently increased ATP production.

MATERIALS AND METHODS

Generation of *Rpl3* and *Rpl3l* knockout mice

Rpl3$^{+/-}$ *and Rpl3l*$^{-/-}$ mice were produced by the Mouse Engineering Garvan/ABR (MEGA) Facility (Moss Vale and Sydney, Australia) using CRISPR/Cas9 [clustered regularly interspaced palindromic repeats (CRISPR)/CRISPR-assocated peptide 9] gene targeting in C57BL/6J mouse embryos following established molecular and animal husbandry techniques (31). The single guide RNAs (sgRNAs) employed were based on the following target sequences [protospacer-associated motif (PAM) italicized and underlined]: *Rpl3* (exon 6) TTCCAGGGGTAACCAGTCGT*TGG* and *Rpl3l* (exon 5) GTGGGCCTTCTTCTGCCGAA*AGG*. To target *Rpl3 or Rpl3l*, 50 zygotes were electroporated in a solution containing the specific sgRNA (300 ng/μl) and Cas9

mRNA (600 ng/μl). Embryo preparation and electroporation was carried out according to the method of Qin *et al*. (32), except that zygotes were incubated for 25 s (not 10 s) in acidic Tyrode's solution and received three (not two) pulses. Microinjected or electroporated embryos were cultured overnight and those that underwent cleavage were introduced into pseudopregnant foster mothers. Pups were screened by polymerase chain reaction (PCR) across the target site and Sanger sequencing of PCR products to detect modifications to the targeted gene. Founders carrying frameshift deletions were backcrossed to wild-type (WT) C57BL/6J mice and heterozygous progeny then inter-crossed. Viable homozygous mice were generated at normal Mendelian frequencies in the case of the $Rpl3l^{\Delta}$ lines whereas homozygous $Rpl3^{\Delta}$ mice all showed pre-natal lethality.

Validation of $Rpl3l^{-/-}$ mice

The CRISPR/Cas9 deletion in the *Rpl3l* gene was validated: (i) at the genomic level using Sanger sequencing, which confirmed that homozygous knockout mice had a 13 bp long deletion in the fifth exon (Supplementary Figure S1B); and (ii) at the mRNA level using single nuclei RNA-sequencing (sNuc-seq), which showed that reads mapping to *Rpl3l* had a 13 bp deletion in $Rpl3l^{-/-}$ hearts (Supplementary Figure S1A). The lack of *Rpl3l* in $Rpl3l^{-/-}$ mice was validated: (i) at the mRNA level using quantitative reverse transcription–PCR (RT–qPCR), which showed that *Rpl3l* was absent in the cytoplasm of striated muscles in $Rpl3l^{-/-}$ mice, but present in WT mice (Figure 2B); and (ii) at the protein level using western blot (Figure 2C), immunofluorescence (Figure 2D) and proteomics (Figure 5B; Supplementary Table S1), confirming the absence of RPL3L (uL3L) in $Rpl3l^{-/-}$ mice.

We should note that our sNuc-seq results showed that both *Rpl3* and *Rpl3l* are being transcribed in both WT and $Rpl3l^{-/-}$ mice hearts, as they can be detected at the mRNA level in the nucleus of both WT and $Rpl3l^{-/-}$ hearts (Supplementary Figure S2A), in agreement with the predicted chromatin states of these genes in heart samples (Supplementary Figure S3). Altogether, our results suggest that the 13 bp deletion in $Rpl3l^{-/-}$ mice leads to degradation of the *Rpl3l* mRNA at the cytosolic level (Figure 2B), and consequently lack of RPL3L (uL3L) protein (Figure 2C, D).

Generation of $Rpl3l^{-/-}$-RiboTag-E2a-Cre mice

RiboTag mice were purchased from The Jackson Laboratory (Stock No. 011029). This mouse line, generated by the McKnight lab (33), carries a floxed WT C-terminal exon in the *Rpl22* gene, followed by a mutant exon that has a triple haemagglutinin (HA) epitope inserted in front of the stop codon, leading to the generation of HA-tagged ribosomes when crossed with a Cre-expressing mouse strain. The RiboTag mice were first crossed with the E2a-Cre mouse line, also purchased from The Jackson Laboratory (Stock No. 003724), and bred to homozygous genotype, ensuring the excision of the WT C-terminal exon and the expression of HA-tagged *Rpl22* in all tissues. These mice were then crossed with the $Rpl3l^{-/-}$ strain and bred to obtain a homozygous genotype.

Mice tissue collection

All experiments were performed with male mice aged between 8 and 10 weeks, unless stated otherwise. All mice were euthanized using CO_2, except for the Ribo-seq, NanoTRAP and sNuc-seq experiments, for which mice were euthanized using cervical dislocation, and tissues were snap-frozen in liquid nitrogen.

Total RNA extraction from mice tissues

Tissues were homogenized in TRIzol (Life Technologies, 15596018) using the Polytron PT 1200 E hand homogenizer in pulses of 10 s at maximum speed until thoroughly homogenized. Total RNA was extracted using ethanol precipitation, and purity and concentration were measured using a NanoDrop spectrophotometer.

Body composition measurements using magnetic resonance imaging (MRI)

The body composition of 8-week-old male and 55-week-old female $Rpl3l^{-/-}$ and $Rpl3l^{+/+}$ mice was analysed using the EchoMRI™-100H Body Composition Analyser without anaesthetizing. The EchoMRI™-100H delivers precise body composition measurements of fat, lean, free water and total water masses in live animals. Statistical significance of the results was assessed using unpaired *t*-test.

Histopathological analyses of $Rpl3l^{-/-}$ knockout and control mice

A complete necropsy of 8-week-old male $Rpl3l^{-/-}$ and $Rpl3l^{+/+}$ mice ($n = 5$) was performed to check for possible macroscopic findings. Mice were weighed before euthanasia with CO_2. The heart and brain were weighed in order to obtain the body weight to organ and brain to organ ratios. The right quadriceps, right gastrocnemius and apex of the heart were embedded in optimal cutting temperature compound (OCT) and were frozen straight away. The left quadriceps, left gastrocnemius and the whole heart (excluding the apex) were collected and fixed in buffered 4% paraformaldehyde overnight, and then transferred to phosphate-buffered saline (PBS). The tissues were then trimmed, paraffin embedded, sectioned (3–4 μm tissue sections) and stained with haematoxylin/eosin (H&E). All the hearts were trimmed transversally at the same level in order to obtain a biventricular short axis section (biventricular, transversal). The proximal area of both the gastrocnemius and quadriceps were trimmed transversally, and the remaining tissue was sectioned longitudinally. At least three cross-sections of each heart were evaluated in a blinded manner in order to detect histopathological changes of the myocardium such as disarray, myocardial degeneration, hypertrophy or atrophy, and other possible alteration such as inflammation or fibrosis. Furthermore, quantitative analysis of the left ventricle, right ventricle and myocardial fibres was performed using the NDP.view 2 2.8.24 software (Hamamatsu). The measurements of the left and right ventricular free walls were performed as previously reported (34), with a single line from the endocardium to the pericardium oriented as

perpendicularly as possible to both surfaces, always at areas without papillary muscle. Five measurements were performed preferably in the same cross-section, except in cases where it was not possible. The muscle samples were evaluated in a blinded manner in order to detect histopathological changes such as sarcoplasmic enlargement or thinning, vacuolization or nuclear centralization (signs of degeneration or atrophy) and other possible alterations such as inflammation or fibrosis. A description of the main histological features present was done using the following semi-quantitative grading system: 1, minimal; 2, mild; 3, moderate; 4, marked; 5, severe.

Echocardiography analyses of *Rpl3l*$^{-/-}$ knockout and control mice

Anaesthesia was induced in mice using 5% isoflurane then they were weighed and transferred to a warming pad (40°C) with built-in ECG for heart rate (HR) determination. The pad is integrated into the Vevo3100 (Fujifilm SonoSite, Inc., WA, USA) ultrasound system. An MX400 probe was used for all assessments. The chest was shaved, washed and ultrasound gel applied. Isoflurane was adjusted to keep the HR as close to 500 beats per minute (BPM) as possible while inhibiting the righting reflex. Systolic function was assessed from single high-resolution ECG gated B-mode cineloops (EKV). Endocardial and epicardial volumes were determined using the bullet formula Vol = 5/6 × L × A, where A is the area determined by planimetry at the mid-papillary level and L is the long axis length from the junction of the aortic leaflets to the apical dimple. Stroke volume (SV) was calculated as the difference between endocardial volumes at end-diastole (ED) and end-systole (ES), EDV and ESV, respectively. Ejection fraction (EF) was calculated as SV/EDV. ED was defined as the beginning of the ECG R-wave upstroke and ES as the closure of the aortic valve. Diastolic function was assessed using pulse-wave and tissue Doppler from an apical four-chamber view of the mitral valve. Left atrial dimension was determined as the diameter along a line aligned to the inferior edge of the aortic annulus in a parasternal long-axis B-mode image at ES. All recorded metrics, for both WT and *Rpl3l*$^{-/-}$ mice, can be found in Supplementary Table S2.

Micromanometry analyses of *Rpl3l*$^{-/-}$ knockout and control mice

Micromanometry was performed 24–48 h after echocardiography in a randomized blinded way. Following anaesthetic induction under 4–5% isoflurane in medical oxygen, mice were laid and secured supine on a pre-warmed mat with a nose cone delivering 1–2% isoflurane. To monitor anaesthesia, pedal reflex and respiration rate were observed. With the head extended, the neck was shaved and washed, then a 1–1.5 cm longitudinal incision to the right of the anterior midline was made. Using blunt dissection, the sternohyoid and sternomastoid muscles were separated to expose the internal right carotid artery posterior and lateral to the trachea. The vessel was isolated with three 4–0 Silk (J&J Inc., NJ, USA) ligatures. The distal end was ligated while the proximal end was looped under the artery; these two were then tensioned against each other while the middle was run loosely twice around the artery. The pre-warmed and calibrated 1.2F Scisence (Transonic Scisense Inc., NY, USA) catheter was dipped in lubricating gel and introduced into the artery via a puncture made using a 32G needle at the distal end, then the middle ligature was tensioned to secure the catheter. With the proximal ligature released, the catheter was progressed into the aortic arch. A characteristic sawtooth signal was observed in the acquisition software display (Acqknowledge Ver 3.8.2. BioPac Systems Inc., CA, USA) and was recorded for several minutes. During this time, the anaesthesia was lightened to allow the HR to increase to ∼500 BPM, before the catheter tip was advanced into the left ventricle and recorded for several minutes before removal. Analysis was performed using the same software, and results can be found in Supplementary Table S2.

RT–qPCR

Total RNA isolated from mouse tissues was used as starting material for qPCRs. Briefly, total RNA was first treated with TURBO™ DNase (Life Technologies, AM2239) for 30 min at 37°C to remove possible DNA contamination. Total RNA was then re-extracted using acid phenol–chloroform (Life Technologies, AM9720) and quantified using a NanoDrop spectrophotometer. A 100 ng aliquot of total RNA was mixed with oligo(dT) primers, random hexamers and 10 mM dNTP mix (Invitrogen, 18080051). The reaction mixture was heated to 65°C in a thermocycler, after which it was quickly chilled on ice. RNase inhibitors (Invitrogen™ RNaseOUT™), 0.1 M dithiothreitol (DTT) and the First-strand buffer (Invitrogen, 18080051) were added to the reaction mixture which was incubated at 42°C for 2 min. SuperScript™ II reverse transcriptase (Life Technologies, 18064–014) was finally added, and the reaction mixture was incubated at 42°C for 50 min, followed by a 15 min inactivation at 70°C. The synthesized cDNA was diluted 1:6 and used for the qPCR. The Power SYBR Green Master Mix (Life Technologies, A25741) was used as the fluorescent dye, and the primers used were as follows: *Rpl3_fw*, GGAAAGTGAAGAGCTTCCCTAAG; *Rpl3_rev,* CTGTCAACTTCCCGGACGA; *Rpl3l_fw*, GAAGGGCCGGGGTGTTAAAG; *Rpl3l_rev*, AGCTCTGTACGGTGGTGGTAA; *GAPDH_fw*, AGCCTCGTCCCGTAGACAAA; *and GAPDH_rev*, AATCTCCACTTTGCCACTGC. All oligonucleotide sequences used in qPCR experiments can be found in Supplementary Table S3. The LightCycler® 480 Instrument II was used for the qPCR with the following program: 90°C, 2 min; 40 cycles of 90°C, 5 s; 60°C, 10 s; 72°C, 20 s.

Quantification of mitochondrial genome copy number

Mitochondrial DNA (mtDNA) quantification was performed according to Quiros *et al*. (35). Briefly, mice were euthanized and hearts were collected and cut into small pieces. Then 10–30 mg of tissue was transferred to an ice-cold 1.5 ml Eppendorf tube and 600 μl of lysis buffer [100 mM NaCl, 10 mM EDTA, 0.5% sodium dodecylsulphate (SDS), 20 mM Tris–HCl pH 7.4] was added, followed by 0.2 mg/ml proteinase K. The samples were incubated

overnight at 55°C. The next day, 100 μg/ml RNase A (Qiagen, 158922) was added and the samples were incubated for 30 min at 37°C. A 600 μl aliquot of ultrapure phenol:chloroform:isoamyl alcohol (25:24:1, v/v/v) was added and mixed well. The samples were centrifuged at 12 000 *g* for 5 min, and the aqueous phase was transferred to a new tube. A 250 μl aliquot of 7.5 M ammonium acetate and 600 μl of isopropanol (0.7 v/v) were mixed well. The samples were then centrifuged at 15 000 *g* for 10 min at 4°C. The supernatant was discarded, and the pellet was washed with 500 μl of 70% ethanol. The pellet was air-dried and resuspended in TE buffer (10 mM Tris–HCl pH 7.4 and 1 mM EDTA). The concentration was measured using NanoDrop and the samples were diluted to 10 ng DNA/μl. qPCR was done as previously described. The primers used were as follows: *mt16S_fw*, CCGCAAGGGAAAGATGAAAGAC; *mt16S_rev*, TCGTTTGGTTTCGGGGTTTC; *Nd1_fw*, CTAGCAGAAACAAACCGGGC; *Nd1_rev,* CCGGCTGCGTATTCTACGTT; *Hk2_fw,* GCCAGCCTCTCCTGATTTTAGTGT; and *Hk2_rev,* GGGAACACAAAAGACCTCTTCTGG.

Polysome profiling

Whole hearts were cut into small pieces and homogenized in pre-chilled 2 ml Eppendorf tubes using a bead beater in ice-cold polysome extraction buffer (PEB), which contained 20 mM Tris–HCl pH 7.4, 200 mM KCl, 10 mM $MgCl_2$, 1 mM DTT, 0.1 mg/ml cycloheximide (CHX), 10 U/ml DNase I (NEB, M0303S), 1× cOmplete™ protease inhibitor cocktail (Roche, 11873580001) and 100 U/ml RNAse inhibitors (RNaseOUT, Invitrogen, no. 18080051) using the following program: two cycles of 15 s, 1 min incubation on ice and one cycle of 30 s. The homogenates were incubated for 5 min on ice and then centrifuged at 20 000 *g* for 12 min at 4°C. Triton X-100 was added to the final concentration of 1%, and the homogenates were incubated for 30 min on an end-over-end rotator at 4 °C. The samples were then centrifuged in a benchtop centrifuge at maximum speed for 12 min and the supernatant was transferred to a new tube. Linear sucrose gradients of 10–50% were prepared using the Gradient Station (BioComp). Briefly, SW41 centrifugation tubes (Beckman Coulter, Ultra-Clear™ 344059) were filled with Gradient Solution 1 (GS1), which consisted of 20 mM Tris–HCl pH 8, 200 mM KCl, 10 mM $MgCl_2$, 0.2 mg/ml CHX and 10% w/v RNase-free sucrose. GS1 and Gradient Solution 2 (GS2) were prepared with RNase/DNase-free UltraPure water and filtered with a 0.22 μm filter. The tube was then filled with 6.3 ml of GS2 layered at the bottom of the tube, which consisted of 20 mM Tris–HCl pH 8, 200 mM KCl, 10 mM $MgCl_2$, 0.2 mg/ml CHX and 50% w/v RNase-free sucrose. The linear gradient was formed using the tilted methodology, with the Gradient Station Maker (BioComp). Once the gradients were formed, 700 μl of each lysate was carefully loaded on top of the gradients, and tubes were balanced in pairs, placed into pre-chilled SW41Ti buckets and centrifuged at 4 °C for 150 min at 35 000 rpm. Gradients were then immediately fractionated using the Gradient Station, and 20 × 500 μl fractions were collected in 1.5 ml Eppendorf tubes while absorbance was monitored at 260 nm continuously. Total proteins were extracted from individual fractions by adding trichloroacetic acid (TCA) to the final concentration of 10% v/v, followed by centrifugation at 4°C at maximum speed for 10 min. The supernatant was discarded, the protein pellets were dissolved in NuPAGE™ LDS Sample Buffer supplemented with NuPAGE™ Sample Reducing Agent, and later used for subsequent western blot analysis.

Puromycin incorporation assay

The mice were euthanized by cervical dislocation, the aortae were clamped using haemostatic forceps and the hearts were quickly excised and placed onto a Petri dish. Puromycin (1.2 μmol; Sigma-Aldrich, P8833) dissolved in PBS was injected per single heart though the left ventricle, and the buffer was reinjected for 20 min. The hearts were snap-frozen and later used for western blot analysis. The anti-puromycin antibody (DSHB, PMY-2A4) was used at a concentration of 0.4 μg/ml.

Isolation of the mitochondrial fraction

The mice were euthanized by cervical dislocation and the hearts were quickly excised and placed into ice cold BIOPS (10 mM Ca-EGTA, 0.1 μM free calcium, 20 mM imidazole, 20 mM taurine, 50 mM K-MES, 0.5 mM DTT, 6.56 mM $MgCl_2$, 5.77 mM ATP, 15 mM phosphocreatine, pH 7.1). Blood clots were carefully removed and the hearts were cut into small pieces using cooled scissors. The tissue was transferred into a 2 ml Dounce homogenizer, and 0.5 ml of isolation buffer (225 mM mannitol, 75 mM sucrose, 1 mM EGTA) was added. The tissue was homogenized at medium speed in 6–8 strokes. The homogenate was transferred to a 1.5 ml tube and centrifuged at 800 *g* for 10 min at 4°C. The supernatant was transferred to a new 1.5 ml Falcon tube, and centrifuged at 10 000 *g* for 10 min at 4°C. The supernatant was saved for subsequent western blot analysis of the cytoplasmic fraction. The mitochondrial pellet was carefully resuspended in 1 ml of isolation buffer and centrifuged at 10 000 *g* for 10 min at 4°C. The supernatant was discarded and the mitochondrial pellet was lysed in 100 μl of ice-cold RIPA buffer. The lysate was used for subsequent western blot analysis.

Protein extraction and western blot

Frozen tissues were chopped into smaller pieces and homogenized in ice-cold RIPA buffer using the Polytron PT 1200 E hand homogenizer in pulses of 10 s at maximum speed until thoroughly homogenized. The homogenates were then agitated on an end-over-end shaker at 4°C for 2 h. Finally, the homogenates were centrifuged for 20 min at 12 000 rpm at 4°C in a microcentrifuge. The supernatant was placed in a new tube and kept on ice, and the pellet discarded. Protein concentration was measured using the Bradford assay, and ∼15 μg of total protein was mixed with the NuPAGE™ LDS Sample Buffer supplemented with NuPAGE™ Sample Reducing Agent, incubated at 70°C for 10 min and loaded onto a 12% polyacrylamide gel. The electrophoresis was run at 80 V until the samples reached the resolving gel, when the voltage was increased to 120

V. The transfer was performed onto a polyvinyldifluoridene (PVDF) membrane in a Bolt™ Mini Gel Tank, at a constant voltage of 20 V for 50 min. The membrane was then washed three times for 5 min in TBS-T (Tris-buffered saline with Tween-20), after which it was blocked for 1 h in 3% bovine serum albumin (BSA) in TBS-T (blocking buffer). The incubation with primary antibodies [RPL3 rabbit polyclonal antibody (Proteintech, 11005–1-AP); RPL3L (uL3L) Rabbit Polyclonal Antibody (custom-made, kindly provided by Professor John McCarthy), RPL7 rabbit polyclonal antibody (Abcam, ab72550) and TOMM20 rabbit polyclonal antibody (Abcam, ab78547)] was performed in blocking buffer overnight at 4°C at a 1:1000 dilution. The next day, the membrane was washed three times for 5 min, and incubated in the secondary horseradish peroxidase (HRP)-coupled antibody (Abcam, ab6721) at a 1:10 000 dilution in blocking buffer for 1 h at room temperature. The membrane was washed three times and imaged using the SuperSignal™ West Pico PLUS Chemiluminescent Substrate. The membrane was then reprobed with an anti-glyceraldehyde phosphate dehydrogenase (GAPDH) antibody (1:1000 in blocking buffer) for 1 h and reimaged the same way. Full images of all western blots shown in this work can be found in Supplementary Figures S4, S5 and S6. We should note that commercially available anti-RPL3L (uL3L) antibodies were also tested (Abcam, ab200646; Biorbyt, orb234958; Sigma-Aldrich, HPA049136) but none of them gave specific bands that were present in WT and absent in *Rpl3l*$^{-/-}$ samples. The custom-made anti-RPL3L (uL3L) antibody used here also has some non-specific bands, but those bands are also present in tissues in which *Rpl3l* is not expressed, such as the liver (Supplementary Figure S4D).

Immunofluorescence assays

Freshly collected heart and muscle tissues were quickly frozen with OCT and cut into 12 μm thick slices using a cryotome. The slices were circled with a hydrophobic marker and incubated with 4% formaldehyde in PBS for 10 min at room temperature. The slides were then washed in PBS in staining jars three times for 5 min. To ensure the permeabilization of the cells, the samples were incubated with 0.5% Triton X-100 in PBS for 30 min at 4°C. Three washes with PBS were repeated, and the tissues were blocked with 3% BSA in TBS-T for 30 min at room temperature. The slides were washed with TBS-T three times for 5 min, and incubated with the primary antibodies [RPL3 rabbit polyclonal antibody (Proteintech, 11005–1-AP); RPL3L rabbit polyclonal antibody (custom-made in the lab of Professor John McCarthy) and anti-Atp5a Mouse Monoclonal Antibody (Abcam, ab14748)] in blocking solution at a dilution of 1:200 (5 μg/ml in the case of anti-Atp5a) overnight at 4°C. The next day, the samples were washed with TBS-T three times for 5 min, and incubated in the secondary antibody mixture [anti-rabbit secondary antibody Alexa Fluor 555 (Thermo Fisher Scientific, A-21429) 1:400, phalloidin-iFluor 488 (Abcam, ab176753) and Hoescht 33342 (Thermo Fisher Scientific, H3570)] 1:1000 in blocking solution] for 1 h at room temperature. The slides were then washed with TBS-T three times for 5 min, air-dried for a few minutes and mounted with coverslips. The immunofluorescence images were made using the Leica TCS SPE confocal microscope.

Luminometry assays for ATP quantification

Cardiomyocytes isolated from WT and *Rpl3l*$^{-/-}$ hearts were diluted to the same concentrations and the cell suspensions were mixed with the same volume of CellTiter-Glo (Promega, G7570), as instructed by the manufacturer. The reaction mixtures were pipetted into wells of an opaque 96-well plate and mixed for 2 min at room temperature, and the luminescence was read using the Berthold LB 960 Microplate Luminometer.

Phylogenetic analysis

To build a phylogenetic tree of the RPL3/RPL3L family, full proteomes of representative species (36) were downloaded from Uniprot. A Hidden Markov Model (HMM) profile of RPL3 (PF00297) was downloaded from Pfam (37), and was used to query the selected proteomes using the hmmsearch function from the HMMER package (version 3.3) (http://hmmer.org/). Hits were then aligned to the HMM using the hmmalign function from HMMER, and a phylogenetic tree was built using the maximum likelihood method of IQ-TREE (version 1.6.11) (38,39). The final tree was visualized using FigTree (version 1.4.4) (http://tree.bio.ed.ac.uk/software/figtree/). The code to reproduce the phylogenetic analyses is available in GitHub: https://github.com/novoalab/RPL3L/tree/main/Phylogeny.

Analysis of ribosomal protein expression patterns across mouse tissues and developmental stages

Previously published RNA-seq data (40) were used for the expression analysis. The RPKM (reads per kilobase of transcript per million reads mapped) values for all tissues across the time series were downloaded from the ArrayExpress EBI repository (https://www.ebi.ac.uk/arrayexpress/files/E-MTAB-6798/E-MTAB-6798.processed.1.zip). RPKM values corresponding to RPs were extracted from the full list, and the median expression values were calculated from biological replicates. The ComplexHeatmap R package was used to construct the heatmaps shown in Figure 1 and Supplementary Figure S7, and the code to reproduce the heatmap figures can be found in GitHub: https://github.com/novoalab/RPL3L/tree/main/ComplexHeatmap.

Ribosome pulldown using anti-HA antibodies (for Nano-TRAP)

The HA-pulldown on *Rpl3l*$^{-/-}$-RiboTag-E2a-Cre and *Rpl3l*$^{+/+}$-RiboTag-E2a-Cre mice hearts was done using a modified approach devised by Sanz *et al.* (41). The mice were euthanized using cervical dislocation, and the hearts were excised, removing the aorta and the atria. The hearts were placed in ice-cold PBS supplemented with 100 μg/ml CHX and the blood was removed by gently squeezing with forceps. While on ice, the hearts were chopped into smaller pieces and added to pre-chilled 2 ml tubes containing ∼100 μl of acid-washed glass beads (425–600 μm) and 1 ml of

homogenization buffer (50 mM Tris–HCl, pH 7.5, 100 mM KCl, 12 mM $MgCl_2$, 1% Nonidet P-40 substitute, 1 mM DTT, 200 U/ml RNasin, 1 mg/ml heparin, 100 μg/ml CHX, 1 × protease inhibitor mixture). The hearts were then homogenized using a Mini Beadbeater (BioSpec Products) in two cycles of 60 s and one cycle of 15 s, allowing the samples to cool down on ice for 1 min between the cycles. The lysates were cleared by centrifuging for 10 min at 10 000 *g* at 4°C. The supernatants were transferred to pre-chilled DNA LoBind tubes, and small aliquots of 40–80 μl were transferred to separate tubes and kept at –80°C for subsequent input analysis. A 4 μl aliquot of anti-HA antibody (BioLegend, 901513) was added to the remaining cleared lysate and incubated for 4 h at 4°C on an end-over-end rotator. Pierce™ Protein A/G Magnetic Beads were resuspended by gentle vortexing and transferred into DNA LoBind tubes. The tubes were placed on a magnetic stand and the storage buffer was discarded. Then 400 μl of the homogenization buffer was added and the tubes were incubated for 5 min on an end-over-end rotator. The beads were collected with the magnetic stand and the buffer was discarded. The cleared lysate and he antibody was added to the beads and incubated overnight at 4°C in an end-over-end rotator. On the next day, the high-salt buffer was prepared freshly (50 mM Tris–HCl, pH 7.5, 300 mM KCl, 12 mM $MgCl_2$, 1% Nonidet P-40 substitute, 0.5 mM DTT, 100 μg/ml CHX). The samples were placed into the magnetic stand and the supernatant removed. A 800 μl aliquot of high-salt buffer was added to tubes to remove non-specific binding from the immunoprecipitates and the tubes were washed for 5 min on an end-over-end rotator at 4°C. The tubes were then placed into the magnetic stand and the supernatant removed. The high-salt washes were repeated twice more, for a total of three washes. In the last washing step, the beads were transferred to a clean tube, and all high-salt buffer was carefully removed. A 350 μl aliquot of RLT buffer from the Qiagen RNeasy extraction kit supplemented with β-mercaptoethanol was added to the tubes, which were then vortexed for 30 s at room temperature. The tubes were placed into the magnetic stand, and total RNA was extracted from the immunoprecipitates following Qiagen's RNeasy extraction kit directions. Total RNA was quantified using Nanodrop and Qubit, and the integrity was assessed using the Tapestation.

Purification of cardiomyocytes from total hearts

The purification of cardiomyocytes from mouse hearts was done according to a protocol published by Acker-Johnson *et al*. (42). Briefly, the mice were anaesthetized with isoflurane and the chest was opened to expose the heart. The descending aorta was cut and the heart was perfused through the right ventricle with 7 ml of EDTA buffer [130 mM NaCl, 5 mM KCl, 0.5 mM NaH_2PO_4, 10 mM HEPES, 10 mM glucose, 10 mM 2,3-butanedione monoxime (BDM), 10 mM taurine, 5 mM EDTA, pH adjusted to 7.8 with NaOH and sterile filtered]. The ascending aorta was clamped using haemostatic forceps, and the heart was excised and submerged in fresh EDTA buffer in a 60 mm dish. The heart was then perfused through the left ventricle with 10 ml of EDTA buffer, 3 ml of perfusion buffer (130 mM NaCl, 5 mM KCl, 0.5 mM NaH_2PO_4, 10 mM HEPES, 10 mM glucose, 10 mM BDM, 10 mM taurine, 1 mM $MgCl_2$, pH adjusted to 7.8 with NaOH and sterile filtered) and 30–50 ml of collagenase buffer (0.5 mg/ml collagenase 2, 0.5 mg/ml collagenase 4, 0.05 mg/ml protease XIV in perfusion buffer, heated to 37°C). Digested hearts were pulled apart into 1 mm pieces using forceps and gently triturated using a P1000 pipette. Digestion was stopped by adding stop buffer [perfusion buffer with 5% foetal bovine serum (FBS)], and the cell suspension was filtered through a 100 μm strainer. The cells were submitted to two rounds of gravitational sedimentation of 15–20 min each, and then used for subsequent analyses.

Preparation of cardiomyocyte ribosomes for mass spectrometry (MS) analysis

After isolating cardiomyocytes from *Rpl3l*$^{-/-}$-RiboTag-E2a-Cre and *Rpl3l*$^{+/+}$-RiboTag-E2a-Cre mice, ribosomes were pulled down using anti-HA antibodies and magnetic beads, as explained above. Ribosomes bound to magnetic beads were washed three times using the high-salt buffer, and then another six times with 200 mM ammonium bicarbonate (ABC; #09830–500G, Sigma, MI, USA) to wash away the detergent. The beads were then resuspended in 6 M urea (#17–1319-01, GE Healthcare, UK), reduced with 30 nmol DTT (#D9163-25G, Sigma) (37°C, 60 min with shaking), alkylated in the dark with 60 nmol iodoacetamide (#D9163-25G, Sigma) (25°C, 30 min) and then diluted to 1 M urea with 200 mM ABC for trypsin digestion (Sequence-grade, #V5111, Promega, WI, USA) (1 μg, at 37°C, overnight with shaking). All buffers were prepared in 200 mM ABC. The beads were separated from the supernatant on a magnet, and the supernatant was acidified with 100% formic acid (#1.00264.0100, Merck, DK). C18 stage tips (UltraMicroSpin Column, #SUM SS18V, The Nest Group, Inc., MA, USA) were then conditioned by adding methanol (#14262, Sigma) and centrifuged at 100 *g* for 5 min. They were then equilibrated by two additions of 5% formic acid and centrifuged as in the previous step. Acidified samples were then loaded onto the columns and centrifuged at 100 *g* for 10 min. The samples were reapplied and the centrifugation step repeated. Three washing steps were performed with 5% formic acid, and the peptides were eluted using 50% acetonitrile (#34967, Sigma) and 5% formic acid. The eluate was vacuum dried and used for subsequent analyses.

Digestion and analysis of cardiomyocyte protein samples using MS

Samples were analysed using a Orbitrap Eclipse mass spectrometer (Thermo Fisher Scientific, San Jose, CA, USA) coupled to an EASY-nLC 1200 [Thermo Fisher Scientific (Proxeon), Odense, Denmark]. Peptides were loaded directly onto the analytical column and were separated by reversed-phase chromatography using a 50 cm column with an inner diameter of 75 μm, packed with 2 μm C18 particles. Chromatographic gradients started at 95% buffer A and 5% buffer B with a flow rate of 300 nl/min and gradually increased to 25% buffer B and 75% A in 79 min and

then to 40% buffer B and 60% A in 11 min. After each analysis, the column was washed for 10 min with 10% buffer A and 90% buffer B. Buffer A: 0.1% formic acid in water. Buffer B: 0.1% formic acid in 80% acetonitrile. The mass spectrometer was operated in positive ionization mode with nanospray voltage set at 2.4 kV and source temperature at 305°C. The acquisition was performed in data-dependent acquisition (DDA) mode and full MS scans with 1 micro scan at a resolution of 120 000 were used over a mass range of m/z 350–1400 with detection in the Orbitrap mass analyser. Auto gain control (AGC) was set to 'auto' and charge state filtering disqualifying singly charged peptides was activated. In each cycle of data-dependent acquisition analysis, following each survey scan, the most intense ions above a threshold ion count of 10 000 were selected for fragmentation. The number of selected precursor ions for fragmentation was determined by the 'Top Speed' acquisition algorithm and a dynamic exclusion of 60 s. Fragment ion spectra were produced via high-energy collision dissociation (HCD) at a normalized collision energy of 28% and they were acquired in the ion trap mass analyser. AGC was set to 2E4, and an isolation window of 0.7 m/z and a maximum injection time of 12 ms were used. Digested BSA (NEB, P8108S) was analysed between each sample to avoid sample carry-over, and to ensure stability of the instrument, and QCloud (43) was used to control instrument longitudinal performance during the project. The MaxQuant software suite (v1.6.0.16) was used for peptide identification and quantification. The data were searched against a Swiss-Prot mouse database (as of June 2020, 17 056 entries) plus Q9CQD0, E9PWZ3, Q3V1Z5 isoforms and a list of common contaminants and all the corresponding decoy entries (44). A precursor ion mass tolerance of 4.5 ppm at the MS1 level was used, and up to two missed cleavages for trypsin were allowed. The fragment ion mass tolerance was set to 0.5 Da. Oxidation of methionine and protein acetylation at the N-terminus were defined as variable modifications, whereas carbamidomethylation on cysteines was set as a fixed modification. Identified peptides and dependent peptides have been filtered using a 5% and 1% false discovery rate (FDR), respectively. Intensities were normalized by the levels of Atp5a1, a mitochondrial protein with similar intensities across all samples, and used to calculate fold change, *P*-value and adjusted *P*-value (FDR) to compare the WT versus the knockout. We manually reviewed the peptides identified 'by matching' corresponding to protein RPL3 in WT samples (FQTMEEK, IGQGYLIKDGK and VAFSVAR). Skyline-daily software (v21.1.1.233) (45) was used to extract the area of these peptides and to confirm that their intensity was much less abundant or absent in WT compared with *Rpl3l*$^{-/-}$ samples, thus most probably representing false-positive matches. Thus, the intensity of the aforementioned peptides assigned 'by matching' was corrected for the analyses and final results. The raw proteomics data have been deposited in the Proteomics Identification Database (PRIDE) (46) repository with the dataset identifier PXD026985.

Poly(A) RNA selection from mouse hearts

Poly(A) selection was performed using Dynabeads Oligo(dT)25 beads (Invitrogen, 61002) starting from either HA-pulldown immunoprecipitated RNA (5–10 μg of input) or total RNA from whole hearts (15 μg of input). The beads were first pelleted on a magnetic stand and resuspended in binding buffer (20 mM Tris–HCl, pH 7.5, 1.0 M LiCl, 2 mM EDTA). The beads were repelleted, the buffer was removed and the beads were resuspended in binding buffer. Total RNA (5–10 μg) in diethylpyrocarbonate (DEPC)-treated water was mixed 1:1 with binding buffer, and the mixture was immediately heated at 65°C for 2 min. The mixture was then added to the beads, mixed thoroughly by pipetting and incubated on the end-over-end rotator for 10 min at room temperature. The samples were placed on the magnet and the supernatant was transferred to a clean tube [for the second round of poly(A) selection]. The beads were washed with washing buffer B (10 mM Tris–HCl, pH 7.5, 0.15 M LiCl, 1 mM EDTA) three times, and the supernatant was removed. The first round of poly(A)-containing RNA was eluted with cold 10 mM Tris–HCl, pH 7.5 by heating the mixture at 75°C for 2 min. The supernatant for the second poly(A) selection was denatured by heating at 65°C for 3 min and immediately placed on ice. The beads were resuspended in lysis/binding buffer (100 mM Tris–HCl, pH 7.5, 500 mM LiCl, 10 mM EDTA, 1% lithium dodecylsulphate (LiDS), 5 mM DTT], placed on the magnet and the supernatant was removed. The denatured RNA was added to the beads, mixed thoroughly by pipetting and incubated on an end-over-end rotator for 10 min at room temperature. The tube was placed on the magnet and the supernatant was discarded. The washing steps and the elution were performed as previously described, and the eluate was mixed with the eluate from the first round. In the case of poly(A) selection from whole hearts, the two eluates were mixed with the beads for a third round.

Nanopore direct cDNA sequencing library preparation

All nanopore sequencing runs were performed using the MinION sequencer (flow cell type: FLO-MIN106, sequencing kit: SQK-DCS109, barcoding expansion kit: EXP-NBD104). Standard Oxford Nanopore direct cDNA sequencing protocol (version DCB_9091_v109_revC_04Feb2019) was used to sequence mouse total RNA heart samples (input) as well as translated fractions (HA-bound). A 100 ng aliquot of poly(A) selected RNA per sample was used for the first-strand synthesis reaction, mixed with 2.5 μl of VNP (ONT cDNA sequencing kit) and 1 μl of 10 mM dNTPs, and filled to 7.5 μl with RNase-free water. The mixture was incubated at 65°C for 5 min and then snap-cooled on ice. The following reagents were mixed in a separate tube: 4 μl of 5× RT buffer, 1 μl of RNaseOUT (Invitrogen™), 1 μl of RNase-free water and 2 μl of Strand-Switching Primer (SSP, ONT cDNA sequencing kit). The tubes were gently mixed by flicking and incubated at 65°C for 2 min. A 1 μl aliquot of Maxima H Minus Reverse Transcriptase (Life Technologies, EP0751) was added to the reaction mixture, which was mixed by flicking and incubated for 90 min at 42°C, followed by heat inactivation at 85°C for 5 min. RNA was degraded by adding 1 μl of RNase Cocktail Enzyme Mix (ThermoFisher, AM2286) followed by incubation for 10 min at 37°C. DNA clean up was performed using AMPure XP beads, and quantity and quality were assessed using Qubit™ and Tapestation™. The second strand was

synthesized by mixing the following reagents: 25 μl of 2× LongAmp Taq Master Mix (NEB, 174M0287S), 2 μl of PR2 primer (ONT cDNA sequencing kit), 20 μl of reverse-transcribed sample and 3 μl of RNase-free water. The reaction mixture was incubated using the following protocol: 94°C, 1 min; 50°C, 1 min; 65°C, 15 min; 4°C, hold. Another AMPure XP beads clean up step was performed, proceeding to the end-prep step by mixing the following reagents: 20 μl of cDNA sample, 30 μl of RNase-free water, 7 μl of Ultra II End-prep reaction buffer (NEB, E7647A) and 3 μl of Ultra II End-prep enzyme mix (NEB, E76468). The mixture was incubated at 20°C for 5 min and 65°C for 5 min. After another AMPure XP beads clean up step, the samples were barcoded by mixing the following reagents: 22.5 μl of End-prepped cDNA, 2.5 μl of native barcode (NB01-NB12, ONT barcode extension kit EXP-NBD104) and 25 μl of Blunt/TA ligase master mix. The reaction mixture was incubated for 10 min at room temperature, and the barcoded samples were cleaned up using AMPure XP beads. The cDNA amounts were measured using Qubit™, and the samples were pooled together in equal ratios, not exceeding 120 ng (200 fmol) as the maximum total amount of barcoded cDNA. The adapter ligation was performed by mixing together 65 μl of the pooled barcoded sample, 5 μl of Adapter Mix II (AMII, ONT cDNA sequencing kit), 20 μl of NEBNext Quick Ligation Reaction Buffer 5X (NEB, B6058S) and 10 μl of Quick T4 DNA Ligase (NEB, M2200L). The reaction mixture was incubated for 10 min at room temperature, after which the cDNA was cleaned up using AMPure XP beads and eluted in 13 μl of Elution Buffer (EB, ONT cDNA sequencing kit). The final amount was ∼50 ng of cDNA, which was mixed with 37.5 μl of Sequencing Buffer (SQB) and 2.5 μl of Loading Beads (LB, ONT cDNA sequencing kit), and loaded onto a previously primed MinION R9.4.1 flowcell.

Analysis of cDNA nanopore sequencing data (Nano-TRAP)

Basecalling and demultiplexing of the raw fast5 files was done using Guppy (version 3.6.1) through the MasterOfPores pipeline (version 1.1) (47). Fastq files were then mapped to the GRCm38 mouse genome, in which all non-protein-coding sequences were previously masked. Mapping was performed using minimap2 (version 2.14) (48). The bam files were used for the subsequent differential expression analysis, and Gencode's M25 mouse release was used as the annotation file. Differential expression analysis of nanopore cDNA sequencing runs (Nano-TRAP input and immunoprecipitation) was performed using bambu (version 0.3.0) (doi: 10.18129/B9.bioc.bambu, pre-publication release). DeltaTE (initial release) was used to compute the translation efficiency (49). All code for analysis of Nano-TRAP data is available at: https://github.com/novoalab/RPL3L/tree/main/bambu and https://github.com/novoalab/RPL3L/tree/main/Nano-TRAP_TE.

Ribosome profiling library preparation

For heart homogenates, mice were sacrificed, and their hearts were quickly excised, washed in PBS containing 100 μg/ml CHX and snap-frozen in liquid nitrogen. Left ventricular tissue was homogenized using a tissue homogenizer in 5 vols of ice-cold polysome buffer (20 mM Tris pH 7.4, 10 mM $MgCl_2$, 200 mM KCl, 2 mM DTT, 1% Triton X-100, 1 U/μl DNase) containing 100 μg/ml CHX and further homogenized using a 25G needle. For complete lysis, the samples were kept on ice for 10 min and subsequently centrifuged at 20 000 *g* to precipitate cell debris, and the supernatant was immediately used in the further steps. From the lysate, 100 μl was used as input, from which RNA was extracted using Trizol. The remaining lysate was used to generate ribosome-protected footprints (RPFs) by treatment with RNase I for 45 min at room temperature. After 45 min, the reaction was stopped by adding SUPERase RNase Inhibitor. RPFs were purified using MicroSpin S-400 columns (Cytiva). Purified RPFs were used for the generation of ribosome profiling libraries using the NEXTFLEX small-RNAseq V3 kit (Perkin-Elmer) according to the user guide. Input RNA libraries were prepared using the NEBNext® Poly(A) mRNA Magnetic Isolation Module (ref. e7490) and NEBNext® Ultra II Directional RNA Library Prep Kit for Illumina (24 reactions ref. e7760 or 96 reactions ref. e7765) according to the manufacturer's protocol, to convert total RNA into a library of template molecules of known strand origin and suitable for subsequent cluster generation and DNA sequencing. For all samples, ribosome profiling library size distributions were checked on the Bioanalyzer 2100 using a high sensitivity DNA assay (Agilent) and input libraries were analysed using Bioanalyzer DNA 1000 or Fragment Analyzer Standard Sensitivity (ref: 5067–1504 or ref: DNF-473, Agilent) to estimate the quantity and validate the size distribution, and were then quantified by qPCR using the KAPA Library Quantification Kit KK4835 (ref. 07960204001, Roche) prior to the amplification with Illumina's cBot. Libraries were sequenced 1 × 50 + 8 bp on Illumina's HiSeq2500.

Ribosome profiling data analysis

Fastq files were processed and analysed using the RiboToolkit (50) and RiboFlow (initial release) followed by RiboR (51) pipelines. RiboToolkit was used to calculate the codon occupancy at A-, E- and P-sites and the translation efficiency. Briefly, cutadapt (version 1.18) (52) was used to trim 5′ and 3′ adapters and to filter out low quality reads. Trimmed fastq files were uploaded to the RiboToolkit website and the analysis was done using default parameters. RiboFlow was used to process the fastq files (trimming, mapping, filtering reads mapping to rRNA and tRNA sequences, aligning to the transcriptome), and the created ribo objects were loaded into RiboR, which was used to produce the 3 nt periodicity plots. Metagene plots were built using the R package ribosomeprofilingQC (https://bioconductor.org/packages/release/bioc/html/ribosomeProfilingQC.html).

Single nuclei RNA-seq library preparation

Single nuclei were obtained from flash-frozen tissues that were dissociated following a previously described method (53). Tissue homogenization was performed using a 7 ml

glass Dounce tissue grinder set (Merck) with eight strokes of a loose and a tight pestle in homogenization buffer (250 mM sucrose, 25 mM KCl, 5 mM $MgCl_2$, 10 mM Tris–HCl, 1 mM DTT, 1× protease inhibitor, 0.4 U/μl RNaseIn, 0.2 U/μl SUPERaseIn, 0.1% Triton X-100 in nuclease-free water). The homogenate was filtered into a 50 ml tube through a 40 μm cell strainer (Corning) and centrifuged (500 *g*, 5 min, 4 °C) to resuspend the pellet in 500 μl of storage buffer (1× PBS, 4% BSA, 0.2 U/μl Protector RNaseIn). Nuclei were stained with NucBlue Live ReadyProbes Reagents (ThermoFisher) and single nuclei were sorted by fluorescence-activated cell sorting (FACS). The obtained tube was centrifuged (500 *g*, 5 min, 4 °C) to produce a pellet of nuclei. Next, 5 μl of the single nuclei suspension were mixed with 5 μl of Trypan Blue and applied to a Countess II to determine the concentration of nuclei. The suspension was adjusted to 800–1400 cells/μl and loaded to the Chip, targeting the recovery of 5000 nuclei per sample. The Chip was processed using the Chromium Controller protocol (10X Genomics). Libraries were prepared following the Chromium Single Cell 3' Reagent Kit's User Guide (10X Genomics) protocol. Libraries were sequenced using the NovaSeq 6000 flowcell (Illumina).

Single nuclei RNA-seq data analysis

Sequenced single nuclei samples were demultiplexed using bcl2fastq (Illumina) and aligned to the annotated mouse reference genome (mm38, Ensembl v98) with CellRanger (v5.0.0) using default parameters and including introns to globally capture expression of pre-mRNA transcripts. Genomic regions corresponding to annotated RP pseudogenes were masked out. Mapped samples were grouped into AnnData objects and analysed by Scanpy v 1.6.0 (54). Doublets were predicted and removed using Solo (score <0.25) (55) and only nuclei with 300–5000 expressed genes were retained. A gene was considered as expressed if at least one unique molecular identifier (umi) was detected in three nuclei. Nuclei with <200 umi or an abnormally high proportion of mitochondrial RNAs (≥10%) or rRNAs (≥40%) were further removed. Next, umi were normalized so that every nucleus has the same total umi count, and nuclei were clustered and visually displayed using the UMAP method (56). Possible sample batches were corrected using Harmony (57). We should note that sNuc-seq captured *Rpl3l* transcripts in nuclei from *Rpl3l*$^{-/-}$ mice (Supplementary Figure S1). However, the 13 bp long deletion in *Rpl3l*$^{-/-}$ cells was confirmed, since no reads were found to span the CRISPR target sequence (Supplementary Figure S1). *Rpl3l* transcripts are not present in cytosolic extracts of *Rpl3l*$^{-/-}$ hearts (Figure 2B), suggesting that they are readily degraded in the cytosol, most probably via nonsense-mediated decay (NMD) mechanisms. The jupyter notebook used for this analysis is available at: https://github.com/novoalab/RPL3L/tree/main/single_nuclei_analysis.

Imputation of mRNA expression levels in sNuc-seq

MAGIC (v. 0.1.0) (58) was used to impute gene expression corrected for dropout and to recover ribosome paralogue pair relationships. MAGIC was run using the table of single nuclei-normalized umi and with default parameters (number of pca components = 20, ka = 10, t = 6).

Animal ethics

All experimental procedures were approved by the Garvan/St Vincent's Hospital Animal Ethics Committee, in accordance with the guidelines of the Australian Code of Practice for the Care and Use of Animals for Scientific Purposes (Project Nos 16/14 and 16/26). All animals were entered into the study in a randomized order and operators were blinded to genotype and treatments.

RESULTS

RPL3L (uL3L) is a vertebrate-specific RP paralogue that is expressed post-natally in cardiomyocytes

Previous works have shown that RP paralogues are not equally expressed across mammalian tissues (10). However, their expression patterns across developmental stages have been much less studied. Here, we examined the dynamics of RP paralogue expression patterns across both tissues and developmental stages using publicly available RNA-seq datasets (40), which included seven major organs (brain, cerebellum, heart, kidney, liver, ovary and testis) from embryos (E10.5–E18.5) and post-natal mice (P0, P3, P14, P28 and P63). We found that most RPs were constitutively expressed in all tissues, in agreement with previous observations, and found that these RPs typically showed relatively stable expression levels across developmental stages (Figure 1A; see also Supplementary Figure S7). In contrast, the expression patterns of RP paralogues fell into one of three possible behaviours: (i) one of the two paralogues is expressed in all tissues, while the other is only expressed post-natally in a single tissue (e.g. *Rpl3–Rpl3l*, *Rpl10–Rpl10l* and *Rpl39–Rpl39l*); (ii) both paralogues are expressed at similar levels across tissues and developmental stages (e.g. *Rpl22–Rpl22l1*); or (iii) one of the paralogues is dominantly expressed across tissues and developmental stages, while the other one is either expressed at lower levels or not expressed at all (e.g. *Rpl7–Rpl7l1*, *Rpl36a–Rpl36al* and *Rps27–Rps27l*) (Figure 1B).

We observed that RP paralogue genes (*Rpl3l*, *Rpl10l* and *Rpl39l*) that displayed tissue-specific expression patterns also followed similar temporal expression patterns across developmental stages, with their expression levels increasing steeply from embryo to post-natal developmental stages. Moreover, in those tissues in which the tissue-specific RP paralogue was expressed, the expression levels of their counterparts (*Rpl3*, *Rpl10* and *Rpl39*) decreased post-natally, coinciding with increased expression levels of their paralogue (Figure 1A), and suggesting a possible regulatory interplay between RP paralogue pairs.

The *Rpl3l* paralogue gene emerged in early vertebrates (Supplementary Figure S8A), and its sequence is relatively similar to that of its paralogue gene *Rpl3* (75% sequence identity at the protein level), with the C-terminus being the most distinct region between the two paralogues (Supplementary Figure S8B). A superimposition of the RPL3L (uL3L) homology model in the ribosome structure shows

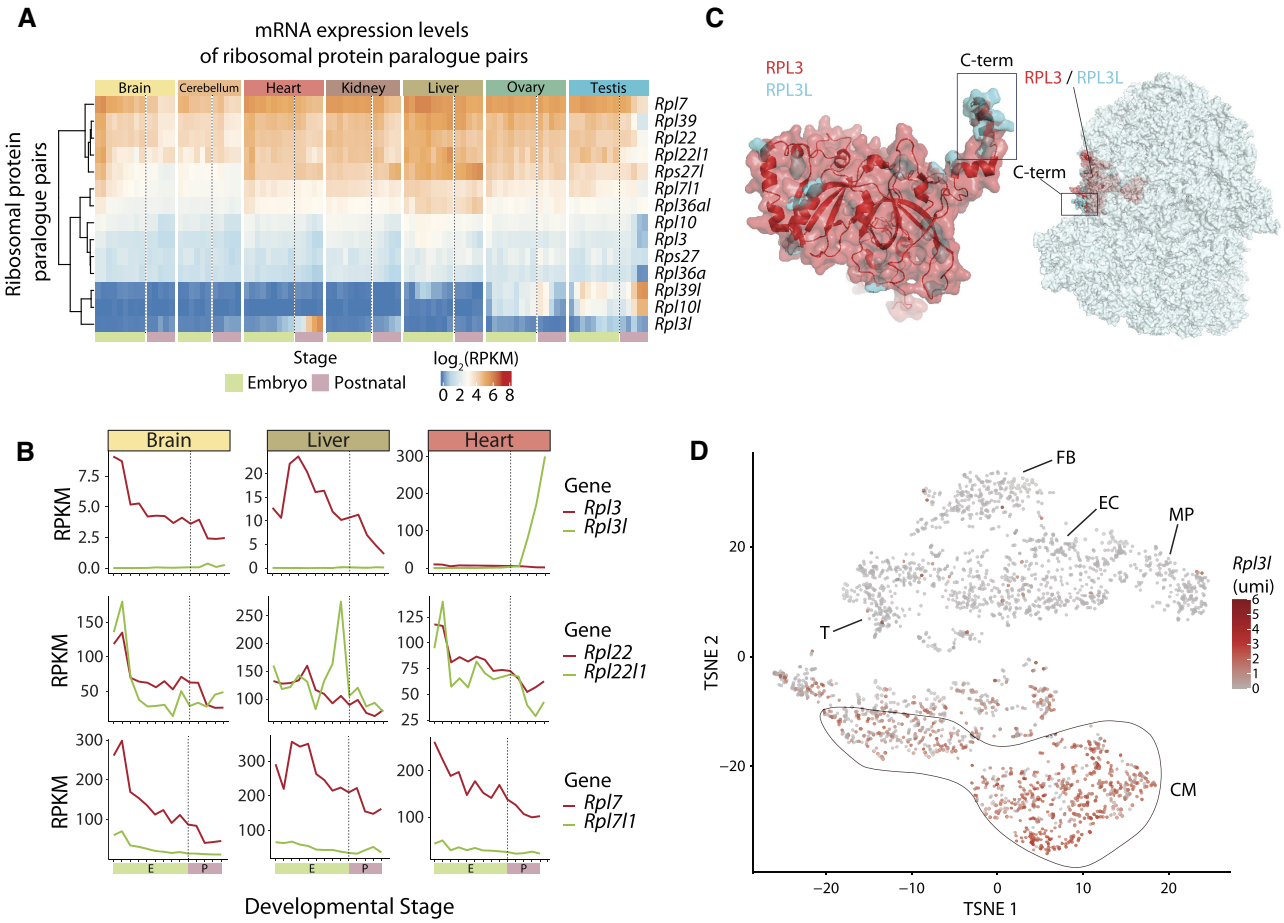

Figure 1. RPL3L (uL3L) is a vertebrate RP paralogue with restricted tissue and developmental expression patterns, such as post-natal expression in mouse cardiomyocytes. (**A**) Heatmap of mRNA expression levels (log RPKM) of ribosomal proteins and their respective paralogues across embryonic (green: E10.5, E11.5, E12.5, E13.5, E14.5, E15.5, E16.5, E17.5 and E18.5) and post-natal mice tissues (pink: P0, P3, P14, P28 and P63). Processed data (RPKM) were obtained from Cardoso-Moreira *et al.* (40). See also Supplementary Figure S7 for a heatmap containing all RPs. (**B**) mRNA expression levels of ribosomal paralogue pairs (RPKM) in three different tissues (brain, liver and heart) for *Rpl3*/*Rpl3l* (upper panel), *Rpl22*/*Rpl22l1* (middle panel) and *Rpl7*/*Rpl7l1* (bottom panel). The developmental stages, shown on the *x*-axis, have been coloured depending on whether they correspond to embryonic (green) or post-natal (pink) stages. (**C**) Structural alignment of human RPL3 (red) and RPL3L (uL3L) (cyan); the C-terminus is highlighted (left) as is the location of RPL3 (uL3)/RPL3L (uL3L) within the ribosome (right). The C-terminus of RPL3 (uL3) and RPL3L (uL3L) is located at the surface of the ribosome, whereas the N-terminus of both proteins lies closer to the peptidyltransferase centre (PTC). The ribosome structure has been obtained from the cryo-electron microscopy structure of the human 80S ribosome, corresponding to PDB code 6IP5 (101), which includes RPL3. The *Homo sapiens* RPL3L (uL3L) structure was obtained from the ModBase (102) database and structurally superimposed to the RPL3 structure in the 80S ribosome. (**D**) T-distributed stochastic neighbour embedding (T-SNE) plot depicting *Rpl3l* expression across mouse heart cell types. Expression data have been extracted from publicly available single-cell RNA-seq data from Ren *et al.* (60). Each dot represents a cell. Expression levels are shown as umi (unique molecular identifiers). Abbreviations: CM, cardiomyocytes; EC, endothelial cells; FB, fibroblasts; MP, macrophage; T, T cells.

that the differential C-terminal region is located on the surface of the ribosome (Figure 1C), suggesting that RPL3L (uL3L)-containing ribosomes could potentially alter the ability of certain accessory proteins to bind to the ribosome, in a similar fashion to what has been previously observed with RPL36- and RPS17-containing ribosomes (59).

To examine in further detail the expression patterns of *Rpl3l*, we used publicly available single-cell RNA-seq data from mouse hearts (60), revealing that the expression of *Rpl3l* in heart tissues is in fact restricted to cardiomyocytes (Figure 1D). Thus, not only is *Rpl3l* expression restricted to specific developmental stages and tissues, but its expression is also limited to myocyte cell types.

Rpl3l knockout mice show up-regulated RPL3 expression in heart and muscle and decreased lean body mass

To reveal the biological function of *Rpl3l*, we generated constitutive knockout mouse models for both *Rpl3* and *Rpl3l* using the CRISPR/Cas9 system (Figure 2A; see also Supplementary Figure S1). Depletion of *Rpl3l* in mice led to viable homozygous knockout mice ($Rpl3l^{-/-}$), with offspring following Mendelian proportions. Knockout of *Rpl3l* was validated at both the mRNA (Figure 2B) and protein level (Figure 2C, D; see also Supplementary Figures S4 and S5). In contrast, depletion of *Rpl3* led to an embryonic-lethal phenotype, and only heterozygous knockout mice ($Rpl3^{+/-}$) could be obtained (see the Materials and Methods).

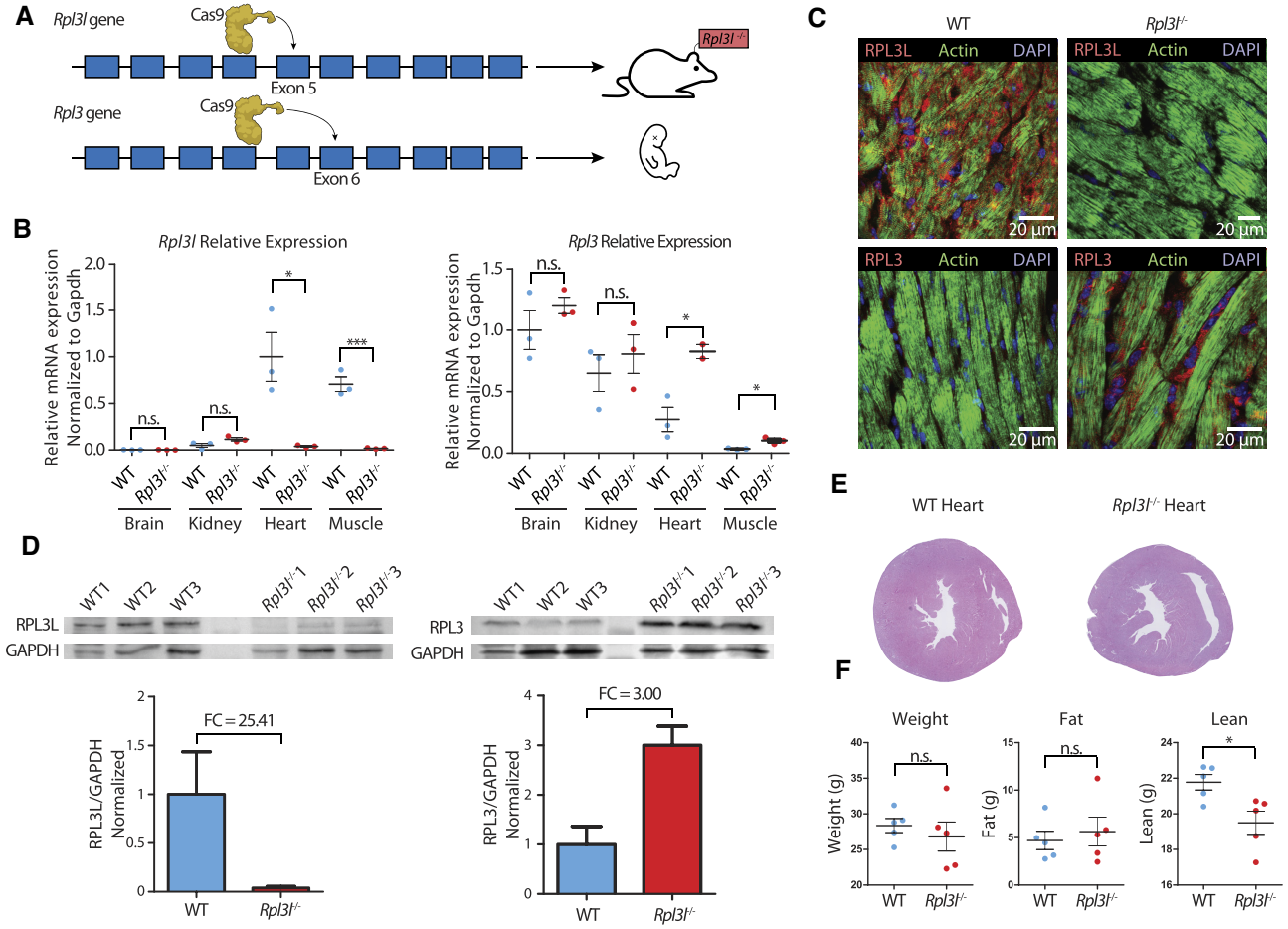

Figure 2. Phenotypic and molecular characterization of *Rpl3l*$^{-/-}$ knockout mice. (**A**) Strategy for generation of *Rpl3*$^{-/-}$ and *Rpl3l*$^{-/-}$ mice using the CRISPR/Cas9 system. *Rpl3l*$^{-/-}$ mice were successfully generated by introducing a 13 bp deletion in exon 5. *Rpl3*$^{-/-}$ mice have an embryonic-lethal phenotype. See also Supplementary Figure S1. (**B**) Relative expression levels of *Rpl3l* (left) and *Rpl3* (right) measured using RT–qPCR and normalized to *Gapdh*. *Rpl3* is ubiquitously expressed, while *Rpl3l* is heart and muscle specific. *Rpl3l*$^{-/-}$ mice do not express *Rpl3l* in any of the tissues ($n = 3$). Statistical significance was assessed using the unpaired *t*-test (*P <0.05, **P <0.01, ***P <0.001). (**C**) Immunofluorescence staining of RPL3 and RPL3L in both WT (left) and *Rpl3l*$^{-/-}$ mice heart tissues (right). Nuclei have been stained with DAPI and are shown in blue; actin is depicted in green and RPL3L (uL3L) (top) and RPL3 (uL3) (bottom) in red. (**D**) Western blot analysis of RPL3L (uL3L) (left) and RPL3 (uL3) (right) in cardiomyocytes isolated from WT and *Rpl3l*$^{-/-}$ hearts ($n = 3$ and $n = 6$, respectively). At the bottom, barplots depicting the fold change of RPL3 (uL3) and RPL3L (uL3L) expression in cardiomyocytes is shown. RPL3L (uL3) and RPL3 (uL3) levels were normalized to GAPDH. See also Supplementary Figure S4 for full blot images, and Supplementary Figure S5 for western blot results using total heart samples from WT and *Rpl3l*$^{-/-}$ mice. (**E**) Representative histological sections of WT and *Rpl3l*$^{-/-}$ heart tissues stained with H&E. A total of 10 mice were included in the histological analyses. See also Supplementary Figure S9. (**F**) EchoMRI analyses of aged (55-week-old) WT and *Rpl3l*$^{-/-}$ mice, in which weight, fat and lean mass were measured for each animal ($n = 5$). Statistical significance was assessed using unpaired *t*-test (*P <0.05).

Histopathological analysis of heart and skeletal muscle tissues (gastrocnemius and quadriceps) from *Rpl3l*$^{-/-}$ mice did not reveal pathological traits or significant morphological changes compared with control *Rpl3l*$^{+/+}$ mice (Figure 2E; see also Supplementary Figure S9A and the Materials and Methods). No statistically significant differences were found between *Rpl3l*$^{-/-}$ and WT mice in heart weight, muscle weight, heart–body weight ratio or heart–brain weight ratio (Supplementary Figure S9B; see also Supplementary Table S4). The left and right ventricular free wall thickness was also found to be non-significant, albeit with a moderate but not significant increase in *Rpl3l*$^{-/-}$ left ventricular free wall thickness (*P*-value = 0.0615). At the physiological level, echocardiographic profiles of *Rpl3l*$^{-/-}$ mice showed no significant differences from those of control *Rpl3l*$^{+/+}$ mice (Supplementary Figure S10; see also Supplementary Tables S2 and S3), except a moderate increase in the rate of pressure generation (dP/dtmax, *P*-value = 0.03). On the other hand, EchoMRI™ analysis of the body composition of live mice showed a significant increase in total lean mass in aged *Rpl3l*$^{-/-}$ knockout mice when compared with age-matched WT mice ($n = 5$ versus 5; *P*-value = 0.02), but not in younger 8-week-old mice ($n = 5$ versus 5; *P*-value = 0.47) (Figure 2F; see also Supplementary Figure S9C and the Materials and Methods).

At the molecular level, we observed that depletion of *Rpl3l* led to a significant increase in *Rpl3* expression levels in heart and skeletal muscle, at both the mRNA (Figure 2B) and the protein level (Figure 2C, D). Thus, a compensatory mechanism in the absence of *Rpl3l* seems to

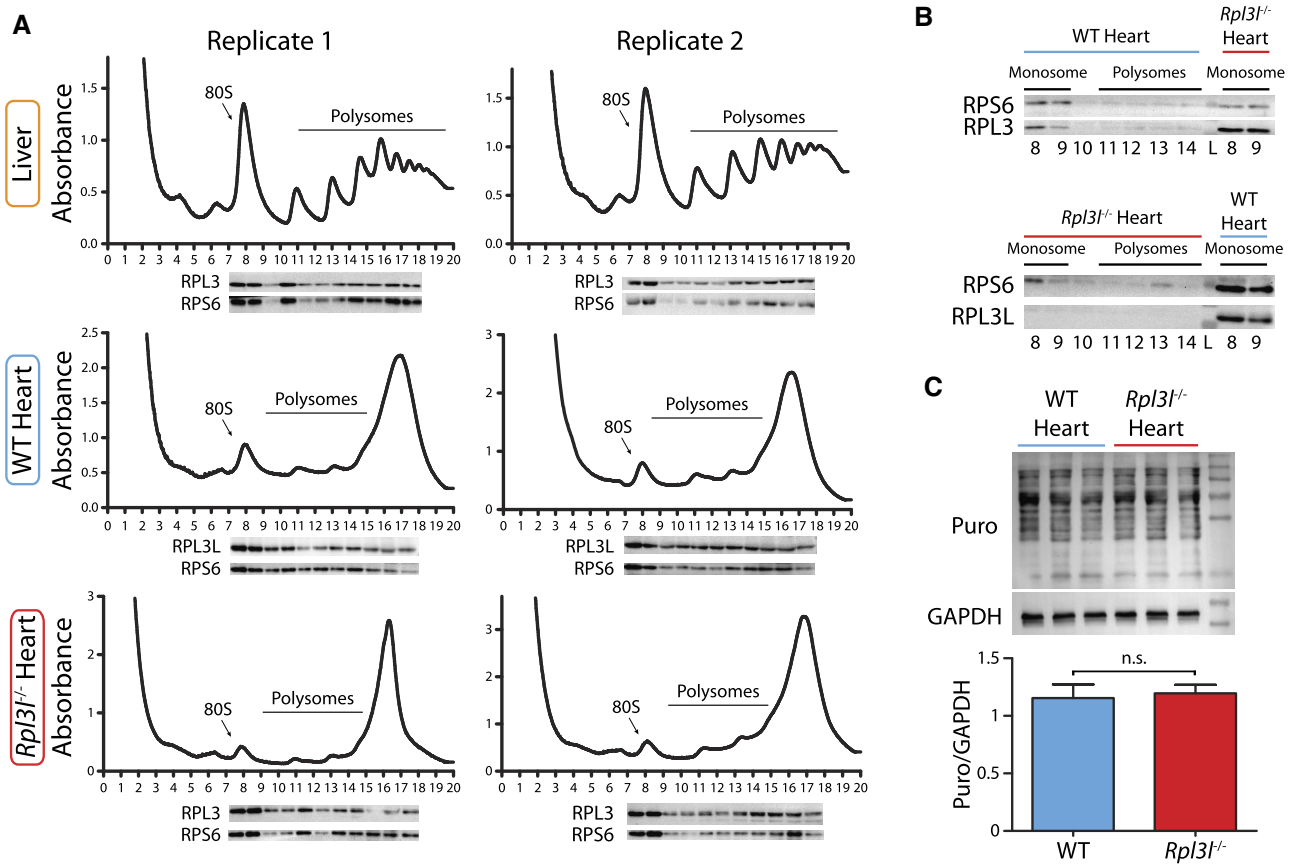

Figure 3. RPL3L and RPL3 are incorporated into translating ribosomes in WT and *Rpl3l*$^{-/-}$ hearts, respectively. (**A**) Polysome profiles of liver (top), WT heart (middle) and *Rpl3l*$^{-/-}$ heart (bottom) were performed in 10–50% sucrose gradients with corresponding western blot analyses, in two biological replicates. Two hearts were pooled together per replicate. Membranes were probed with anti-RPL3L (uL3L), anti-RPL3 (uL3) and anti-RPS6 (eS6) antibodies to show the incorporation of both paralogues in translating ribosomes. (**B**) Polysome profiles fractions of a WT heart (top) and an *Rpl3l*$^{-/-}$ heart (bottom), analysed with western blot and probed with anti-RPL3L (uL3L), anti-RPL3 (uL3) and anti-RPS6 (eS6). Fractions 8 and 9, corresponding to the monosome peak of the polysome profile, of a *Rpl3l*$^{-/-}$ heart and WT heart, respectively, were used as positive controls. (**C**) Puromycin incorporation assay performed on WT and *Rpl3l*$^{-/-}$ hearts in biological triplicates. GAPDH was used as loading control and for normalization in the densitometric analysis. Statistical significance was assessed using unpaired *t*-test. Puro stands for puromycin.

be present in cardiomyocytes, leading to the production of RPL3-containing ribosomes in cardiomyocytes, a cell type where RPL3-containing ribosomes are normally not present post-natally. This biological compensation provides a biological setup that allows for a functional comparative study of the ribosomal activity of RP paralogues in cardiomyocytes, i.e. by comparing the translational activity of cardiomyocytes with RPL3L-containing ribosomes (in WT mice) or RPL3-containing ribosomes (in *Rpl3l*$^{-/-}$ mice), respectively.

RPL3L and RPL3 are incorporated into translating ribosomes

RPL3 (uL3) is a highly conserved core ribosomal protein, and it is well documented that the incorporation of RPL3 (uL3) into ribosomes is of paramount importance for their function (61) (Figure 1D). Even though RPL3L has been described as a tissue-specific paralogue of RPL3, whether it is actually incorporated into translating ribosomes remains elusive.

To examine the incorporation of RPL3L and RPL3 into translating ribosomes in WT and *Rpl3l*$^{-/-}$ cardiomyocytes, respectively, we performed sucrose gradient fractionation of polysome extracts from WT and *Rpl3l*$^{-/-}$ mice hearts coupled to western blotting (Figure 3). Liver was used as a positive control, due to its characteristic and reproducible polysome profiles (Figure 3A, top). Protein content was extracted from each polysome fraction, and the fractions were analysed using western blot, by probing them with anti-RPL3L (uL3L), anti-RPL3 (uL3) and anti-RPS6 (eS6) antibodies. Our results showed that RPL3L (uL3L) is found in the monosome and polysome fractions, demonstrating that RPL3L (uL3L) is incorporated into translating ribosomes (Figure 3A, middle). Moreover, we observed that upon RPL3L (uL3L) depletion, RPL3 (uL3) compensates for the missing paralogue by replacing it in the 60S subunit, and is incorporated into translating ribosomes from *Rpl3l*$^{-/-}$ hearts (Figure 3A, bottom). As additional control, WT and *Rpl3l*$^{-/-}$ heart polysome profile fractions were inversely probed with anti-RPL3 and anti-RPL3L (uL3L) antibodies, respectively, showing that RPL3 (uL3) is also incorporated into monosomes isolated from a whole WT

heart, albeit at lower levels when compared with monosomes of an *Rpl3l*$^{-/-}$ heart (Figure 3B, top). RPL3 signal in WT hearts most probably arises from ribosomes present in non-cardiomyocyte cell types in the heart, as shown in expression profiles obtained using single-cell RNA-seq (Figure 1D). Conversely, RPL3L (uL3L) was not detected in any of the *Rpl3l*$^{-/-}$ polysome profile fractions (Figure 3B, bottom).

Finally, we wondered whether the incorporation of RPL3 (uL3) and RPL3L (uL3L) into actively translating ribosomes might lead to global changes in protein translation. To explore this, we performed puromycin incorporation assays (62) on hearts from WT and *Rpl3l*$^{-/-}$ mice. Analyses of puromycin incorporation levels did not show significant differences, suggesting that the distinct use of RP paralogues, namely RPL3L (uL3L) in WT mice and RPL3 in *Rpl3l*$^{-/-}$ mice, does not globally affect protein translation rates of heart tissues (Figure 3C).

The use of RPL3L does not lead to preferential translation or enhancement of translation efficiency

Previous works have shown that heterogeneity in RP composition endows ribosomes with differential selectivity for translating subpools of transcripts including those controlling metabolism, the cell cycle and development (7). Specifically, it was found that RPL10A- and RPS25-bearing ribosomes showed preferential translation of subsets of transcripts when compared with the whole ribosome population. However, it is unclear whether the use of RP paralogues would lead to preferential translation of specific subsets of transcripts.

Here we examined this question by testing whether RPL3L (uL3L)-containing ribosomes showed preferential translation of subsets of transcripts, relative to RPL3 (uL3)-containing ribosomes. To this end, we devised a novel method, which we termed Nano-TRAP: HA-tag mediated Translating Ribosome Affinity Purification (TRAP) (63) coupled to nanopore cDNA sequencing (Figure 4A; see also the Materials and Methods). Nano-TRAP captures full-length mRNAs that are associated with at least one 80S ribosome. We applied Nano-TRAP in biological triplicates to mouse hearts that were isolated from either *Rpl22*-HA$^{+/+}$/*Rpl3l*$^{-/-}$ or control *Rpl22*-HA$^{+/+}$/*Rpl3l*$^{+/+}$ hearts corresponding to mRNA populations that are bound to RPL3 (uL3)- and RPL3L (uL3L)-containing ribosomes, respectively. We first examined the replicability of Nano-TRAP, finding that per-gene log2-counts across biological replicates were highly replicable (Pearson $r^2 = 0.886$–0.939) (Supplementary Figure S11A, B). We then performed differential expression analysis (see the Materials and Methods) to examine whether the ribosome-bound mRNA populations would be significantly distinct upon knockout of *Rpl3l*, finding only five differentially bound transcripts (Figure 4B; see also Supplementary Table S5). Our results identified *Rpl3* as one of the differentially bound mRNAs, in agreement with our previous results that showed up-regulation of *Rpl3* upon *Rpl3l* depletion (Figure 2B). In addition to increased binding to *Rpl3* transcripts, RPL3L (uL3L)-depleted ribosomes showed significantly decreased binding towards two genes: *Rbp7* and *Ankrd1*, the latter encoding a transcription factor whose dysregulation has been associated with several types of cardiomyopathies (64,65) including hypertrophic cardiomyopathy.

Finally, we examined whether translation efficiency would be significantly altered upon *Rpl3l* depletion. Translation efficiency was calculated by dividing normalized counts from the immunoprecipitation (IP) experiment by those from the input experiment. We then compared the translation efficiency values between WT and *Rpl3l*$^{-/-}$ strains; however, most transcripts did not show significant changes in their translation efficiency values (Figure 4C; see also Supplementary Table S5), and the few genes that showed significant translation efficiency changes were not enriched for any Gene Ontology (GO) term (Supplementary Table S6). Altogether, our analyses using Nano-TRAP suggest that the use of RPL3L (uL3L) instead of RPL3 (uL3) in translating ribosomes does not globally lead to preferential translation of subsets of transcripts in mouse hearts.

Rpl3l depletion does not affect the distribution of ribosomes along transcripts

It has been reported that RPL3, which is located close to the peptidyltransferase centre in the ribosome, plays a role in preventing ribosomes from piling up in the mRNA 5′ region early during translation elongation (61). Therefore, we wondered whether the presence of RPL3 (uL3) or RPL3L (uL3L) in ribosomes might lead to changes in the distribution of ribosomes along specific transcripts.

To examine this, we performed ribosome profiling (Ribo-seq) (66) in WT and *Rpl3l*$^{-/-}$ mouse hearts (Figure 4D; see also Supplementary Figure S12), in biological triplicates, finding a consistent 3 nt periodicity in RPF libraries in all samples (Supplementary Figure S13A). We first examined whether the depletion of *Rpl3l* led to accumulation of reads in specific genic regions. To this end, we analysed the distribution of reads of RPFs at the metagene level; however, we did not observe statistically significant differences between WT and *Rpl3l*$^{-/-}$ RPF reads, finding that reads mapped in similar proportions to the 3′-untranslated region (UTR), CDS and 5′-UTR (Figure 4E). Similarly, metagene analyses showed that RPFs did not accumulate in specific regions of the transcript (Figure 4F; see also Supplementary Figure S14).

We then assessed whether Ribo-seq, when integrated with RNA-seq, would be able to identify transcripts with differential mRNA expression levels (input mRNA), ribosomal occupancy (RFP) or translation efficiency. No significant changes were observed, which suggests that *Rpl3l* depletion did not globally lead to changes in transcription, translation or translation efficiency (Figure 4G), in agreement with our previous observations using Nano-TRAP. Finally, we examined whether RPL3 (uL3)- and RPL3L (uL3L)-containing ribosomes would show differences in ribosome codon occupancies; however, we did not find significant differences between WT and *Rpl3l*$^{-/-}$ hearts (Figure 4H; see also Supplementary Figure S13B).

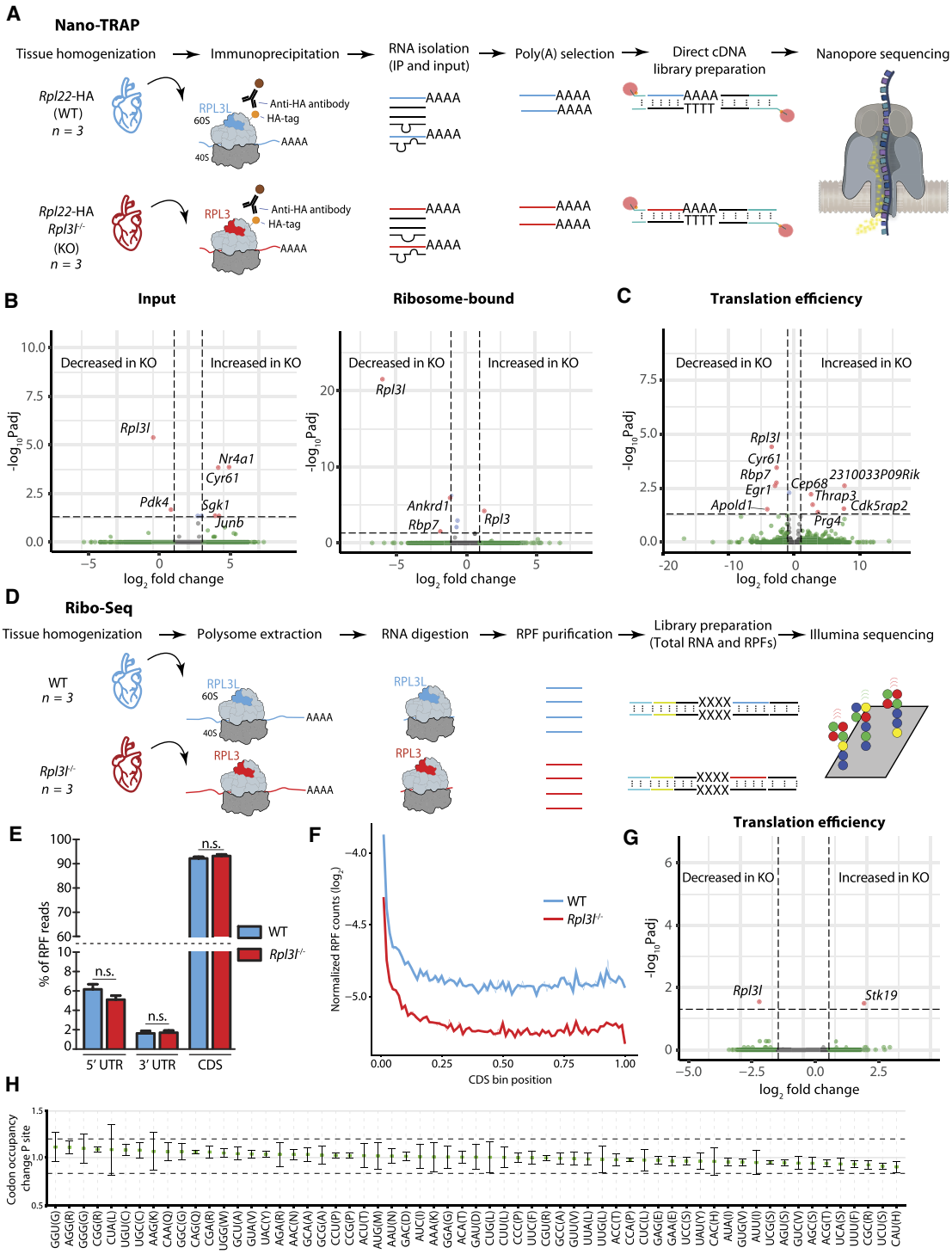

Figure 4. RPL3L usage does not lead to preferential translation or altered translation efficiency. (**A**) Schematic representation of the Nano-TRAP method. (**B**) Volcano plots representing differentially expressed input mRNA (left) and ribosome-bound mRNA (right) transcripts identified using Nano-TRAP, which correspond to those with a fold change >1 and an FDR-adjusted *P*-value <0.05. Nano-TRAP results show minor differences in transcripts captured in RPL3L (uL3L)- and RPL3 (uL3)-bearing ribosomes. Each dot represents a gene, and they have been coloured depending on: (i) adjusted *P*-value <0.05 and fold change >1 (red); (ii) only fold change >1 (green) or only adjusted *P*-value <0.05 (blue); or (iii) neither fold change >1 nor adjusted *P*-value <0.05 (grey). See also Supplementary Table S5. (**C**) Translation efficiency analysis using NanoTrap. Counts were normalized by the sum of counts for each sample. Every dot represents a gene. See also Supplementary Table S5. (**D**) Schematic representation of the Ribo-seq method. (**E**) Percentage of RPF reads mapping to the 5′-untranslated region (UTR), 3′-UTR, and the coding sequence (CDS) of identified genes. The values shown are the mean of three biological replicates. Error bars represent the standard deviation. Statistical significance was assessed using the unpaired *t*-test (**P* <0.05). (**F**) Metagene analysis of RPF reads from WT and *Rpl3l*$^{-/-}$ hearts. (**G**) Analysis of differential translation efficiency, calculated as the ratio between RPFs and mRNAs (see the Materials and Methods), between WT and *Rpl3l*$^{-/-}$ ribosomes. See also Supplementary Table S13. (**H**) Codon occupancy change between WT and *Rpl3l*$^{-/-}$ at the P-site.

Rpl3l expression is mutually exclusive with *Rpl3* expression in cardiomyocytes

Our results show that *Rpl3l* depletion leads to up-regulation of *Rpl3* expression levels, which is concordantly detected at both the mRNA (Figures 2B and 4B; see also Supplementary Figure S15) and protein levels (Figure 2C, D). Intrigued by this compensatory mechanism, we performed sNuc-seq (67–69) on left ventricles from *Rpl3l*$^{+/+}$ and *Rpl3l*$^{-/-}$ mice, in biological triplicates. Compared with single-cell RNA-seq, sNuc-seq improves the profiling of gene expression in cells which are difficult to dissociate from tissues (69).

Analyses of sNuc-seq datasets confirmed that depletion of *Rpl3l* showed no major transcriptomic changes in cardiomyocytes (Supplementary Table S7), in agreement with our previous observations (Figure 4B; Supplementary Figure S10C). Moreover, we confirmed that *Rpl3l* is cardiomyocyte specific, whereas *Rpl3* is mainly expressed in non-cardiomyocyte cells (Supplementary Figure S16A). To examine the interplay between *Rpl3* and *Rpl3l* expression in cardiomyocytes, we imputed gene expression levels across all the identified single nuclei (see the Materials and Methods), finding that *Rpl3* and *Rpl3l* are expressed in a mutually exclusive manner (Supplementary Figure S16B; Supplementary Table S8). In contrast, this mutual exclusivity was not observed in any of the other RP paralogue pairs expressed in the heart (Supplementary Figures S2 and S16C). Altogether, our results suggest that the presence of RPL3L (uL3L) in cardiomyocytes is directly responsible for the lack of RPL3 (uL3) in a given cell.

RPL3-bearing ribosomes establish physical contact with mitochondria

Our analyses show that *Rpl3* and *Rpl3l* protein-coding sequences significantly differ in their C-terminal region (Supplementary Figure S8A), which protrudes towards the outer region of the ribosome (Figure 1C). We therefore reasoned that the incorporation of RPL3L (uL3L) or RPL3 (uL3) in ribosomes could lead to the recruitment of different ribosome-associated proteins (RAPs) (59), which could in turn alter the function or fate of the ribosome.

In order to study how *Rpl3l* depletion affects ribosomal protein composition, we employed antibody IP [pull-down of RPL22-(eL22)-HA-tagged ribosomes from WT or *Rpl3l*$^{-/-}$ cardiomyocytes, respectively] coupled to MS, which we termed Proteo-TRAP (Figure 5A). Our results confirmed that RPL3L (uL3L) was depleted from *Rpl3l*$^{-/-}$ cardiomyocytes at the protein level, while RPL3 was up-regulated (Figure 5B; see also Supplementary Table S1). The only other RP that was significantly over-represented in *Rpl3l*$^{-/-}$ cardiomyocytes was RPL38, suggesting that the *Rpl3l* knockout does not globally lead to substantial alterations in terms of ribosomal protein composition (Supplementary Table S9).

To our surprise, RPL3-containing ribosomes isolated from *Rpl3l*$^{-/-}$ cardiomyocytes showed a dramatic enrichment in interactions with mitochondrial proteins. In contrast, this enrichment was absent in WT cardiomyocytes, which have RPL3L (uL3L)-containing ribosomes (Figure 5C; see also Supplementary Figure S17). GO term enrichment analysis (70) confirmed that interacting proteins were significantly enriched for mitochondria-related molecular functions and biological processes (Figure 5D). We reasoned that the presence of mitochondrial proteins could be caused by increased physical contact between RPL3 (uL3)-containing ribosomes and mitochondria, relative to RPL3L (uL3L)-containing ribosomes. In this regard, it has been shown that in yeast, ribosomes can localize to the outer mitochondrial membrane, supporting co-translational transport of mitochondrial proteins into the mitochondria (71), with electron cryo-tomography images supporting this hypothesis (72). Moreover, it is well documented that mammalian mitochondria also contain ribosome receptors on their outer membrane (73). To examine whether RPL3 (uL3)- and RPL3L (uL3L)-containing ribosomes might show distinct subcellular localizations, we performed western blot analyses of cytosolic and mitochondrial fractions of WT and *Rpl3l*$^{-/-}$ hearts, and found that RPL3 localized to both the cytosolic and the mitochondrial fraction, while RPL3L (uL3L) was almost exclusively detected in the cytosolic fraction (Figure 5E). Thus, we conclude that RPL3-containing ribosomes show altered subcellular localization relative to RPL3L (uL3L)-containing ribosomes, causing an increased presence of mitochondrial proteins upon ribosome pulldowns.

Previous works have shown that RPs, including RPL3 (uL3), can be SUMOylated post-translationally (74,75). In this regard, we observed that the RPL3 (uL3) protein that is located in the mitochondrial fraction was of slightly larger size that found in the mitochondrial fraction (∼46 kDa) (Figure 5E; see also Supplementary Figure S6). However, the addition of SUMO would account for an ∼10 kDa difference, which is larger than the ∼3 kDa that we observed (Supplementary Figure S6B). Thus, RPL3 (uL3) could be a target of as yet uncharacterized post-translational modifications, which could account for the observed size difference between the cytosolic and mitochondrial forms. Alternatively, distinct isoforms could be present in mitochondrial-bound RPL3 (uL3) relative to cytosolic RPL3 (uL3).

Finally, we examined whether the change in subcellular localization towards the mitochondria would be accompanied by altered mitochondrial function. To this end, we performed luminometric measurement of ATP levels in WT and *Rpl3l*$^{-/-}$ cardiomyocytes, finding a significant increase in ATP production upon RPL3L (uL3L) depletion (Figure 5F). We should note that this global increase in ATP levels was not caused by increased abundance of mitochondria in RPL3L (uL3L)-depleted cardiomyocytes (Supplementary Figure S18). Future work will be needed to better comprehend how the increased presence of ribosomes bound to the mitochondria leads to increased mitochondrial function.

Hypertrophy leads to increased *Rpl3* and decreased *Rpl3l* levels in the heart

Cardiac hypertrophy is an adaptive response to pressure or volume stress, mutations of certain proteins or loss of contractile cardiac mass from prior infarction (76). Hypertrophy can occur as a compensatory consequence of pressure

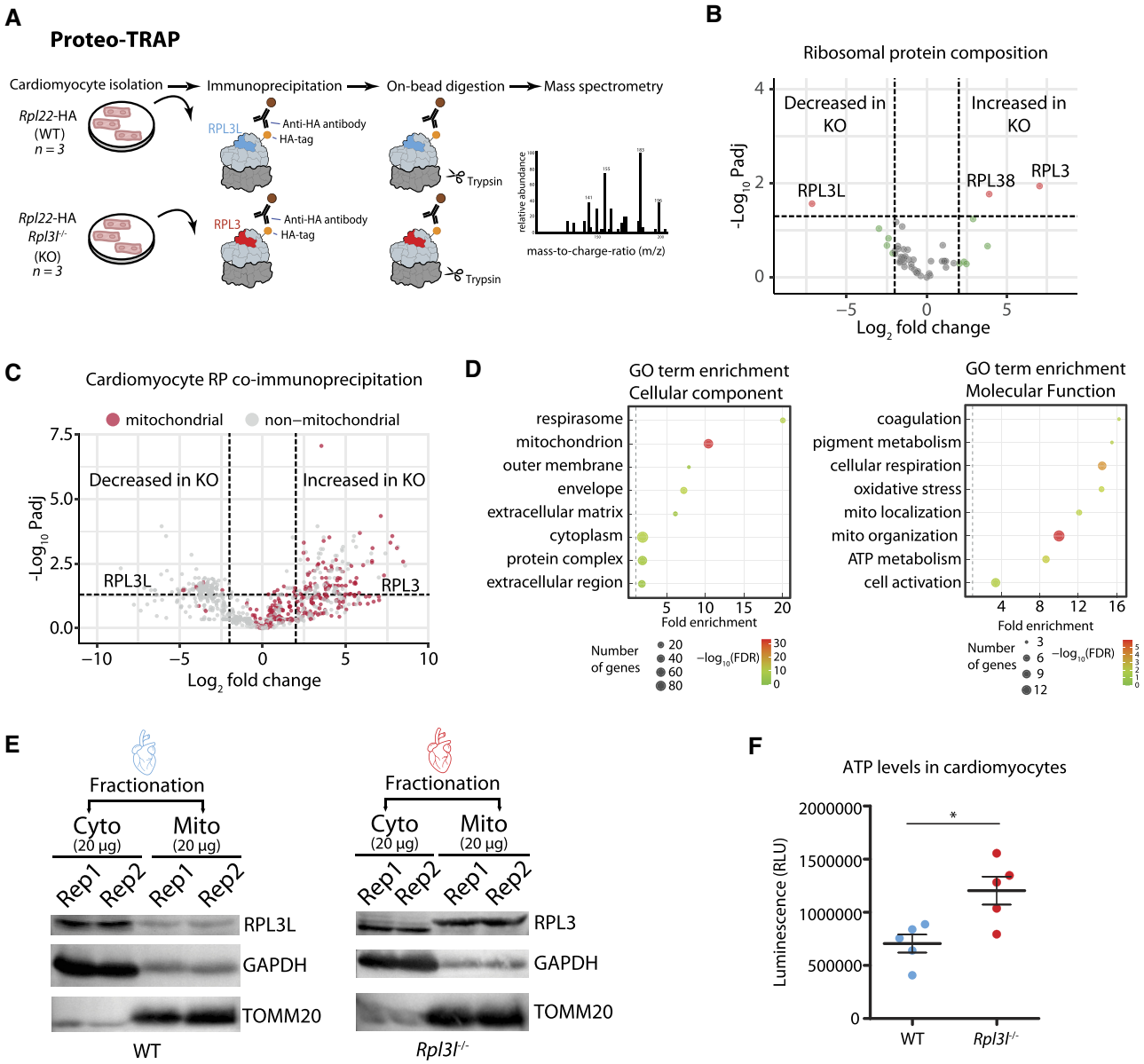

Figure 5. RPL3 (uL3)-containing ribosomes establish physical contact with mitochondria. (**A**) Schematic representation of the Proteo-TRAP method. (**B**) Analysis of differential ribosome composition in cardiomyocytes from WT and *Rpl3l*$^{-/-}$ mice. See also Supplementary Table S9. (**C**) Volcano plot showing mitochondrial (red) and non-mitochondrial (grey) proteins co-precipitating with ribosomes in WT and *Rpl3l*$^{-/-}$ cardiomyocytes. See also Supplementary Table S14 and Supplementary Figure S17. (**D**) GO term enrichment plots showing top hits for cellular components (left) and molecular function (right). (**E**) Western blot analysis of cytosolic and mitochondrial fractions of WT (left) and *Rpl3l*$^{-/-}$ (right) hearts. GAPDH and TOMM20 were used as cytosolic and mitochondrial fraction markers, respectively. See also Supplementary Figure S17 for full membrane images with marker sizes. (**F**) Luminometric measurement of ATP levels in WT and *Rpl3l*$^{-/-}$ cardiomyocytes. Statistical significance was assessed using unpaired *t*-test (*P <0.05).

overload; however, recent studies raise the prospect of modulating hypertrophy to afford clinical benefit without provoking haemodynamic compromise (77,78). To accomplish this goal, it is essential to identify the molecular events that distinguish pathological hypertrophy versus physiological hypertrophy.

Previous works have shown that, in skeletal muscle, hypertrophy leads to increased *Rpl3* and decreased *Rpl3l* mRNA levels (15). Thus, we wondered whether a similar phenomenon may also occur in the hypertrophic heart. To this end, we examined RP mRNA expression levels upon hypertrophic stimuli using publicly available RNA-seq datasets (60,79,80). Analysis of scRNA-seq datasets from resting and hypertrophic hearts [2, 5, 8 and 11 weeks after transverse aortic constriction (TAC) surgery] (60) revealed that *Rpl3l* levels in cardiomyocytes steadily decrease upon a hypertrophic stimulus, with *Rpl3l* being almost undetectable at week 11 (Figure 6A; see also Supplementary Figure S19). Similar results were observed when examining RP expression patterns in bulk RNA-seq data from TAC-induced hypertrophic and control hearts (79). Specifically, *Rpl3*/*Rpl3l* mRNA ratios were consistently altered

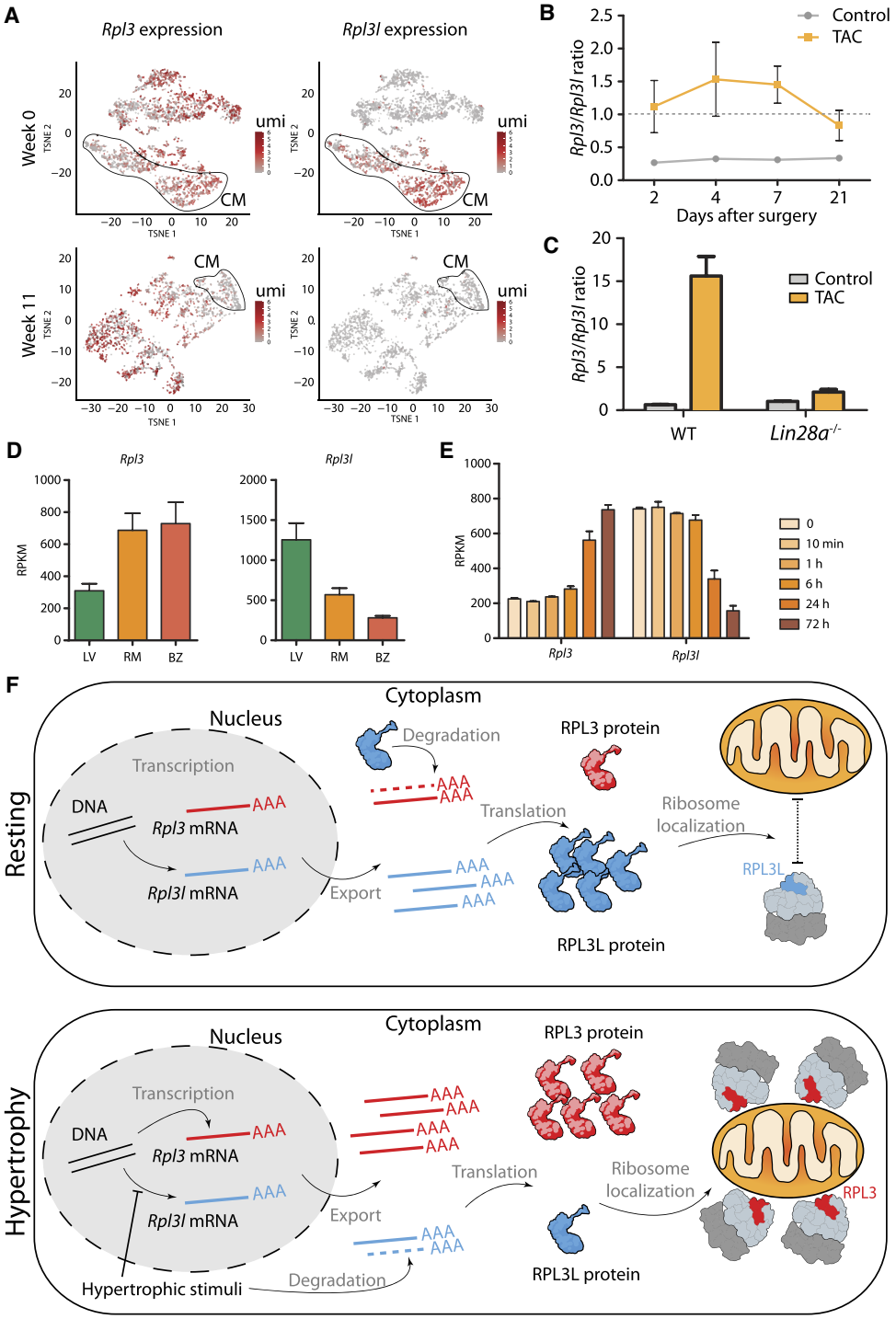

Figure 6. Pressure overload leads to an increase in *Rpl3* expression and a decrease in *Rpl3l* expression in the heart. (**A**) The expression of *Rpl3* and *Rpl3l* across cell types in mouse hearts before (week 0) and after hypertrophy (week 8) induced by transverse aortic constriction (TAC). Cardiomyocytes (CM) are circled. Expression levels are shown as umi (unique molecular identifiers). (**B**) TAC leads to heart hypertrophy that correlates with increased *Rpl3* expression and decreased *Rpl3l* expression. The *Rpl3*/*Rpl3l* ratio is significantly increased at all time points (2, 4, 7 and 21 days after surgery) when compared with control hearts. See also Supplementary Figures S19 and S20 and Supplementary Table S15. (**C**) Effects of TAC-induced hypertrophy on *Rpl3*–*Rpl3l* interplay are impaired in *Lin28a*$^{-/-}$ mice. See also Supplementary Figure S22. (**D**) *Rpl3* (left) and *Rpl3l* (right) nuclear mRNA levels in cardiomyocytes from the left ventricle (LV), remote myocardium (RM) and border zone (BZ) after myocardial infarction. Processed data (RPKM) were obtained from Günthel *et al.* (81). (**E**) *Rpl3* and *Rpl3l* mRNA expression levels at different time points (0 min, 10 min, 1 h, 6 h, 24 h and 72 h) after myocardial infarction. Processed data (RPKM) were obtained from Liu *et al.* (82). (**F**) Model showing the *Rpl3*–*Rpl3l* interplay in resting (top) and hypertrophic (bottom) conditions. In the resting heart, *Rpl3l* is predominantly expressed in cardiomyocytes, and the RPL3L protein negatively regulates *Rpl3* expression, while RPL3L (uL3L)-containing ribosomes do not establish close contact with mitochondria. Upon hypertrophic stimuli, *Rpl3l* expression is impaired and *Rpl3l* mRNA is degraded in the cytoplasm, leading to an increased expression of *Rpl3*. RPL3 (uL3)-containing ribosomes establish close contact with mitochondria.

at all time points after surgery (2, 4, 7 and 21 days) (Figure 6B), while this trend was not seen in other RP paralogue pairs (Supplementary Figures S20 and S21). Finally, we examined whether the interplay between *Rpl3* and *Rpl3l* might be altered upon knockout of *Lin28a* (80), an RNA-binding protein that directly binds and increases mitochondrial phosphoenolpyruvate carboxykinase 2 (*Pck2*) mRNA levels, which has been shown to play an important role in maintaining cardiac hypertrophy (80). Indeed, we found that upon *Lin28a* knockout, the interplay between *Rpl3* and *Rpl3l* expression patterns upon hypertrophic stimulus was impaired (Figure 6C; see also Supplementary Figure S22).

We then wondered whether other heart-related conditions, such as myocardial infarction, may be accompanied by a switch in *Rpl3*/*Rpl3l* expression patterns. To this end, we analysed RNA-seq data performed on cardiomyocyte nuclei isolated from hearts after myocardial infarction (81), finding that *Rpl3* levels were increased both in the 'border zone' (the region most affected by the infarction) and in the 'remote myocardium' (mildly affected by the infarction), relative to the left ventricle (unaffected heart region) (Figure 6D). The increase in *Rpl3* levels was accompanied by a decrease in *Rpl3l* levels in the infarcted areas, suggesting that the *Rpl3*–*Rpl3l* transcriptional switch occurs not only upon hypertrophy, but also upon infarction. Analysis of a second RNA-seq dataset consisting of a time-course of mouse hearts induced with myocardial infarction (82) revealed that the *Rpl3*–*Rpl3l* switch is already detectable at 6 h post-infarction, while the maximal change in *Rpl3*–*Rpl3l* levels was observed 72 h post-infarction (Figure 6E). Altogether, our results point to a molecular interplay between *Rpl3* and *Rpl3l* in cardiomyocytes upon hypertrophic stimuli (Figure 6F) and infarction, suggesting that *Rpl3l* holds promise as a potential target for therapeutic intervention.

DISCUSSION

In recent years, compelling evidence has accumulated supporting ribosome composition heterogeneity (2,7,9,10,83–85). At the level of protein composition, ribosomes lacking specific RPs have been shown to exist within mouse embryonic stem cells (7,9), yeast (3,17,18,86) and bacteria (19), though questions remain as to the functionality of such ribosomes (11). At the level of rRNAs, several studies have shown that these can be expressed from separate genomic loci, with the resulting rRNA molecules differing significantly in their sequences. For example, zebrafish express rRNAs from two separate loci: one locus serves for maternal rRNA transcription and the other for zygotic rRNA (87). Similarly, in *Plasmodium falciparum*, different diverging copies of rRNA are encoded in the genome, one of which is utilized during the mosquito stage and another during the human stage of the infection (88,89).

RP paralogues are present in a wide range of species, but their use as a source of ribosome heterogeneity, as well as their functional relevance, remains unclear. In vertebrates, RP paralogues are believed to have appeared via duplication of the ancestral RP gene (90), can show constitutive or restricted tissue expression profiles (10,90) and their depletion or mutation can lead to tissue-specific phenotypes (91,92). In the case of mice, we find seven RP paralogues, which display 39–99% sequence identity to their ancestral gene (Supplementary Table S10). Here, we examined the functional relevance of RP paralogues in mammals by focusing on the biological role of RPL3L (uL3L) in mice, to unveil why striated muscles in vertebrates evolved to express a distinct version of RPL3, a core RP essential for ribosomal function. Our findings point to a highly specialized function of RPL3L (uL3L), with its expression being tightly regulated at the temporal level (post-natal expression), restricted to few cell types (myocytes) and in limited subsets of tissues (striated muscles) (Figure 1A, D). Moreover, we find that the C-terminus of RPL3L (uL3L) is the most distinct region when compared with RPL3 (Figure 1B; see also Supplementary Figure S8B), which is well conserved among mammalian RPL3L (uL3L) proteins (Supplementary Figure S8C), suggesting its importance to fulfil its specialized function.

By generating *Rpl3* and *Rpl3l* knockout mouse models, we found that ubiquitously expressed *Rpl3* is of paramount importance for mouse development, with homozygous *Rpl3* knockout being embryonic lethal. We should note that this is not the case for other constitutively expressed RP protein genes, such as *Rpl22* (93). In contrast, we successfully generated *Rpl3l*$^{-/-}$ homozygous knockout mice, and identified a rescue mechanism in which RPL3 expression levels are upregulated in striated muscles upon *Rpl3l* depletion (Figure 2B–D; see also Supplementary Figure S5). *Rpl3l*$^{-/-}$ mice showed no apparent histological or physiological aberrations (Supplementary Figure S9), with no significant differences in their echocardiogram profiles when compared with age-matched WT mice (Supplementary Table S11; Supplementary Figure S10). In contrast, 55-week-old *Rpl3l*$^{-/-}$ mice had significantly lower lean mass when compared with age-matched WT mice (Figure 2F), suggesting that RPL3L (uL3L) might be important for muscle maintenance with ageing.

Previous work had already reported an inverse correlation of *Rpl3* and *Rpl3l* expression upon muscle hypertrophy (15), which we also observed upon *Rpl3l* knockout (Figure 2B–D; see also Supplementary Figure S15); however, it remains unclear whether RPL3L (uL3L) is incorporated into translating ribosomes, as its putative role could be exclusively extraribosomal. To test this, we performed polysome profiling coupled to western blot analysis on WT and *Rpl3l*$^{-/-}$ hearts, showing that RPL3L (uL3L) is incorporated into polysomes in WT hearts, while it is substituted by RPL3 (uL3) in *Rpl3l*$^{-/-}$ hearts (Figure 3). Therefore, *Rpl3l* knockout mice offer a model system in which cardiomyocyte ribosomes incorporate RPL3 (uL3) instead of RPL3L (uL3L), thus allowing us to study how the use of RPL3 (uL3) or RPL3L (uL3L) in the ribosome influences translation in i*n vivo* mouse models. We should note that neither induced pluripotent stem cell-derived myocytes nor neonatal myocytes can be used as a model system to study the RPL3 (uL3)–RPL3L (uL3L) interplay that occurs upon hypertrophy as RPL3L (uL3L) is not expressed in embryonic or neonatal myocytes (40).

To examine the molecular function of RPL3L (uL3L) *in vivo*, we first performed Ribo-seq experiments on both WT and *Rpl3l*$^{-/-}$ hearts, finding that the use of RPL3- or RPL3L-containing ribosomes did not lead to altered trans-

lation efficiency of subsets of transcripts (Figure 4G). To confirm these observations, we devised a novel method to study preferential translation, consisting of ribosome pull-down (using HA-tagged ribosomes) coupled to nanopore direct cDNA sequencing, which we termed Nano-TRAP. Ribo-seq is a well-established method that relies on sequencing of RPFs using short-read sequencing technologies; ∼30 nucleotide-long RPFs allow for analyses at the subcodon resolution, but such short fragments also lead to multi-mapping issues, as well as loss of isoform-specific information. On the other hand, Nano-TRAP relies on long-read sequencing, allowing for the analysis of full transcripts and per-isoform analyses, alleviating the mappability problems of RPFs. Furthermore, Nano-TRAP could also be customized for direct RNA sequencing instead of direct cDNA sequencing, allowing for translatome-wide analysis of mRNA modifications.

Our Nano-TRAP analyses confirmed that *Rpl3l* depletion does not lead to preferential translation of transcripts (Figure 4C), in agreement with our observations using Ribo-seq. Therefore, both orthogonal methods show that *Rpl3l* depletion does not lead to global accumulation of ribosome footprints along the transcript or preferential translation of subsets of transcripts, compared with WT samples. We should note that our datasets were not significantly different in terms of coverage from previously published datasets (94), for which we successfully identified differential translation of subsets of transcripts when using the same bioinformatic pipeline (Supplementary Table S12; see also Supplementary Figure S23), suggesting that sequencing coverage was not a limiting factor in the identification of differentially translated transcripts in our experiments.

We then investigated whether the stoichiometry of RPs or RAPs might be altered upon *Rpl3l* depletion. To this end, we performed proteomic analyses of ribosome immunoprecipitates (Proteo-TRAP), in a similar fashion to previous works employing FLAG-tagged ribosomes coupled to MS analyses (7). Unexpectedly, we found a drastic enrichment of genome-encoded mitochondrial proteins in RPL3 (uL3)-containing ribosome immunoprecipitate fractions, compared with RPL3L (uL3L)-containing fractions (Figure 5C). The fact that such a large number of mitochondrial proteins were found in ribosome immunoprecipitates in RPL3 (uL3)-containing ribosomes ($Rpl3l^{-/-}/Rpl22HA^{+/+}$) but not in RPL3L (uL3L)-containing ribosomes ($Rpl3l^{+/+}/Rpl22HA^{+/+}$), despite stringent washing steps (see the Materials and Methods), suggests a strong physical contact between RPL3-containing ribosomes and mitochondria.

It is well documented that ribosomes can bind to the outer mitochondrial membrane, allowing for co-translational transport of mitochondrial proteins encoded by the nuclear genome (73). Such findings have been further corroborated by visualization of cytosolic ribosomes on the mitochondrial surface by electron cryo-tomography (72). In yeast, OM14 has been identified as the mitochondrial receptor of the nascent chain-associated complex, allowing for the binding of ribosomes on the mitochondrial surface (71). In agreement with these observations, previous studies in yeast have shown that certain strains deficient in specific RP paralogues (*Rpl1b*, *Rpl2b* and *Rps26b*) display altered mitochondrial morphology and function (24). Moreover, RPL3 (uL3), in its ribosome-free form, has been shown to have the ability to localize to mitochondria (95). Based on these previous observations, we speculated that the incorporation of RPL3 into cardiomyocyte ribosomes might lead to tighter ribosome–mitochondria interactions, compared with RPL3L (uL3L)-containing ribosomes, potentially affecting mitochondrial function. To test this, we performed western blot analyses of mitochondrial and cytosolic fractions of WT and $Rpl3l^{-/-}$ hearts, finding that RPL3L (uL3L) is only detected in the cytosolic fraction, whereas RPL3 localizes both to the cytosolic and to the mitochondrial fractions (Figure 5E). We then tested whether the localization of RPL3-containing ribosomes to mitochondria affected their function, finding that the use of RPL3 in ribosomes (present in $Rpl3l^{-/-}$ cardiomyocytes) was accompanied by a significant increase in ATP levels (Figure 5F), compared with WT cardiomyocytes with RPL3L (uL3L)-containing ribosomes. Future work will be needed to further dissect how the *Rpl3*–*Rpl3l* interplay regulates mitochondrial activity.

Previous studies focusing on hypertrophy have shown that *Rpl3l* mRNA levels decrease and *Rpl3* mRNA levels increase in muscle upon hypertrophic stimulus (15), supporting its importance in muscle function. Similarly, our analyses using publicly available RNA-seq datasets showed that *Rpl3l* is down-regulated in cardiomyocytes upon hypertrophic stimuli (Figure 6A–C; see also Supplementary Figure S19) as well as upon myocardial infarction (Figure 6D, E). Therefore, our *Rpl3l* knockout mouse models may constitute a promising *in vivo* model to study hypertrophy and myocardial infarction. Notably, a recent study showed that knockdown of *Rpl3l* improved muscle function (96), but the underlying molecular mechanism remains unclear. We propose that the improved muscle function observed in these studies (15,96) might be a direct consequence of altered mitochondrial activity upon *Rpl3l* down-regulation, in a similar fashion to what we observe upon *Rpl3l* depletion (Figure 5F).

The dynamic interplay between mammalian RP paralogues is not an exclusive feature of the *Rpl3*–*Rpl3l* pair, but has also been reported to occur in other paralogue pairs, such as the *Rpl22*–*Rpl22l1* pair. Specifically, homozygous depletion of *Rpl22* in mice is compensated by an up-regulation of its paralogue RPL22L1 (eL22L1) (93), which is otherwise largely absent in its protein form in most adult tissues (Figure 1A). Intrigued by this molecular interplay, we examined previously published genome-wide epigenetic chromatin states (97) of distinct RP paralogue pairs across a wide variety of tissues, finding that both *Rpl3* and *Rpl3l* show active transcription chromatin states in adult striated muscle tissues but not in other tissues (Supplementary Figure S3), suggesting that both genes are actively transcribed and, therefore, that the interplay between *Rpl3* and *Rpl3l* most probably occurs at the mRNA level. In agreement with these observations, a recent study in yeast showed that the interplay between *Rpl22a* and *Rpl22b* occurred at the mRNA level, where the RPL22A (eL22) protein was shown to bind the intron of the unspliced *Rpl22b* RNA transcript, causing its degradation (98). We speculate that a similar regulatory mechanism could be present in vertebrates, and

could potentially explain how the *Rpl3–Rpl3l* interplay that occurs upon hypertrophic stimuli is achieved (Supplementary Figures S20 and S21).

RPL3 (uL3) is a highly conserved core RP that plays an important role in ribosome function, and mutation of key residues of yeast RPL3 (uL3) has been shown to cause altered peptidyltransferase activity and frameshifting efficiency (99). On the other hand, methylation of H243 in *Saccharomyces cerevisiae* has been shown to affect translation elongation and translational fidelity (100). More recently, studies in yeast have shown that the mutation of W255, the residue that is closest to the peptidyltransferase centre, affected diverse aspects of ribosome biogenesis and function (61). Thus, we speculate that while the selective use of RPL3 (uL3) and RPL3L (uL3L) in cardiomyocytes does not affect translation efficiency, it might be affecting translational fidelity. Future work will be needed to decipher whether the incorporation of RPL3 (uL3) or RPL3L (uL3L) into ribosomes might be significantly affecting translational fidelity in mammals.

Altogether, our work shows that *Rpl3l* is a cell type-specific paralogue of *Rpl3* that is restricted to myocyte cells in adult striated muscle tissues, which is down-regulated upon hypertrophic stimuli. We show that although RPL3L (uL3L) is incorporated into actively translating ribosomes, it does not lead to preferential translation or to altered translation efficiency, as demonstrated by Ribo-seq and Nano-TRAP. In contrast, we show that the use of RPL3L (uL3L) or RPL3 (uL3) modulates the subcellular location of ribosomes and mitochondrial activity in cardiomyocytes. Our work expands our understanding of mammalian RP paralogues and their functional relevance *in vivo*, supporting the view that ribosome heterogeneity is accompanied by functional specialization.

DATA AND CODE AVAILABILITY

Nano-TRAP (IP and Input) and Ribo-seq (RPF and mRNA) FASTQ files have been deposited in the Gene Expression Omnibus (GEO), under accession codes GSE189872 and GSE189854, respectively. Single nuclei RNA-seq data have been deposited in the European Nucleotide Archive (ENA) at EMBL-EBI, under accession number PRJEB49255. Proteomics data have been deposited in the Proteomics Identification Database (PRIDE), under accession code PXD026985. A complete list of samples and corresponding codes can be found in Supplementary Table S12. Raw immunofluorescence images have been deposited in Figshare (https://doi.org/10.6084/m9.figshare.19617165.v1). All scripts used in this work, including those used to perform single-cell data analysis, Nano-TRAP analyses, Ribo-seq analyses, phylogenetic trees and heatmaps of RP expression patterns, have been made publicly available in GitHub (https://github.com/novoalab/RPL3L) and Zenodo (https://doi.org/10.5281/zenodo.7418059).

SUPPLEMENTARY DATA

Supplementary Data are available at NAR Online.

ACKNOWLEDGEMENTS

We thank all the members of the Novoa lab for their valuable insights and discussion. We thank Dr Elisenda Sanz Iglesias for her invaluable insights regarding the RiboTag mice; Dr Rob Brink for all his help and discussions on diverse strategies to obtain the CRISPR knockout mice strains used in this work; Professor John McCarthy for providing us with an aliquot of the RPL3L (uL3L) antibody, as well as for insightful discussions on the role of RPL3L (uL3L); Professor Dr Antonio Zorzano and Dr David Sebastián for the discussions and insights regarding mitochondrial biology; Dr Jorge Ferrer for providing us with a cre mouse line; Oliver Hummel for his help uploading the generated sNuc-seq datasets to the European Nucleotide Archive (ENA) repository; and Ana Arsenijevic for her help with the PyMOL structures.

Author contributions: I.M. performed most of the experiments and bioinformatic analyses described in this work, including mouse tissue collection and colony management, mice genotyping, cardiomyocyte preparations, total RNA and protein extractions, western blotting, immunofluorescence assays, polysome profiling, immunoprecipitation, nanopore sequencing, Nano-TRAP and Ribo-seq data analyses. H.G.S.V. performed sucrose gradients, characterized RP antibodies across tissues and contributed to the set up of mouse tissue polysome profiles. M.C.L. contributed to mouse tissue collections and cardiomyocyte isolations. G.P. built the sc-NucRNA libraries, and J.R. performed the sc-nucRNAseq data analyses, which were supervised by N.H. and S.v.H. S.K. and J.W. performed echocardiography experiments, which were supervised by M.F. G.E. and E.S. performed mass spectrometry experiments. M.V. built the Ribo-seq libraries. E.M.N. conceived and supervised the work. I.M. and E.M.N. wrote the manuscript, with the contribution from all authors.

FUNDING

The European Union's Horizon 2020 Research and Innovation Program under the Marie Skodowska-Curie grant agreement [713673]; the Australian Research Council [DE170100506 to E.M.N.]; the Spanish Ministry of Economy, Industry and Competitiveness (MEIC) [PGC2018-098152-A-100 to E.M.N.]; the European Union Horizon 2020 Research and Innovation Program ERC advanced grant [AdG788970 to N.H.] and ERC starting grant [StG101042103 to E.M.N.]; the Leducq Foundation [16CVD03 to N.H.]; the Chan Zuckerberg Foundation [2019-20266 to N.H.]; and 'la Caixa' INPhINIT PhD fellowship [LCF/BQ/DI18/11660028 to I.M.]. We acknowledge the support of the MEIC to the EMBL partnership, Centro de Excelencia Severo Ochoa and CERCA Programme/Generalitat de Catalunya. The CRG/UPF Proteomics Unit is part of the Spanish Infrastructure for Omics Technologies (ICTS OmicsTech) and it is a member of the ProteoRed PRB3 consortium which is supported by grant PT17/0019 of the PE I + D + i 2013-2016 from the Instituto de Salud Carlos III (ISCIII) and ERDF.

Conflict of interest statement. E.M.N. has received travel expenses from ONT to participate in nanopore conferences.

I.M. has received a travel bursary from ONT to present his work in international conferences. E.M.N. is Scientific Advisory Board member for IMMAGINA Biotech. The authors declare that they have no competing interests.

REFERENCES

1. Genuth,N.R. and Barna,M. (2018) The discovery of ribosome heterogeneity and its implications for gene regulation and organismal life. *Mol. Cell*, **71**, 364–374.
2. Kondrashov,N., Pusic,A., Stumpf,C.R., Shimizu,K., Hsieh,A.C., Ishijima,J., Shiroishi,T. and Barna,M. (2011) Ribosome-mediated specificity in Hox mRNA translation and vertebrate tissue patterning. *Cell*, **145**, 383–397.
3. Komili,S., Farny,N.G., Roth,F.P. and Silver,P.A. (2007) Functional specificity among ribosomal proteins regulates gene expression. *Cell*, **131**, 557–571.
4. Mauro,V.P. and Edelman,G.M. (2002) The ribosome filter hypothesis. *Proc. Natl Acad. Sci. USA*, **99**, 12031–12036.
5. Williams,M.E. and Sussex,I.M. (1995) Developmental regulation of ribosomal protein L16 genes in *Arabidopsis thaliana*. *Plant J.*, **8**, 65–76.
6. Kearse,M.G., Chen,A.S. and Ware,V.C. (2011) Expression of ribosomal protein L22e family members in *Drosophila melanogaster*: rpL22-like is differentially expressed and alternatively spliced. *Nucleic Acids Res.*, **39**, 2701–2716.
7. Shi,Z., Fujii,K., Kovary,K.M., Genuth,N.R., Röst,H.L., Teruel,M.N. and Barna,M. (2017) Heterogeneous ribosomes preferentially translate distinct subpools of mRNAs genome-wide. *Mol. Cell*, **67**, 71–83.
8. Sugihara,Y., Honda,H., Iida,T., Morinaga,T., Hino,S., Okajima,T., Matsuda,T. and Nadano,D. (2010) Proteomic analysis of rodent ribosomes revealed heterogeneity including ribosomal proteins L10-like, L22-like 1, and L39-like. *J. Proteome Res.*, **9**, 1351–1366.
9. Slavov,N., Semrau,S., Airoldi,E., Budnik,B. and van Oudenaarden,A. (2015) Differential stoichiometry among core ribosomal proteins. *Cell Rep.*, **13**, 865–873.
10. Guimaraes,J.C. and Zavolan,M. (2016) Patterns of ribosomal protein expression specify normal and malignant human cells. *Genome Biol.*, **17**, 236.
11. Ferretti,M.B. and Karbstein,K. (2019) Does functional specialization of ribosomes really exist?*RNA*, **25**, 521–538.
12. Gerst,J.E. (2018) Pimp my ribosome: ribosomal protein paralogs specify translational control. *Trends Genet.*, **34**, 832–845.
13. Gilbert,W.V. (2011) Functional specialization of ribosomes?*Trends Biochem. Sci.*, **36**, 127–132.
14. Guo,H. (2018) Specialized ribosomes and the control of translation. *Biochem. Soc. Trans.*, **46**, 855–869.
15. Chaillou,T., Zhang,X. and McCarthy,J.J. (2016) Expression of muscle-specific ribosomal protein L3-like impairs myotube growth. *J. Cell. Physiol.*, **231**, 1894–1902.
16. Khatter,H., Myasnikov,A.G., Natchiar,S.K. and Klaholz,B.P. (2015) Structure of the human 80S ribosome. *Nature*, **520**, 640–645.
17. Samir,P., Browne,C.M.,,Rahul, Sun,M., Shen,B., Li,W., Frank,J. and Link,A.J. (2018) Identification of changing ribosome protein compositions using mass spectrometry. *Proteomics*, **18**, e1800217.
18. Collins,J.C., Ghalei,H., Doherty,J.R., Huang,H., Culver,R.N. and Karbstein,K. (2018) Ribosome biogenesis factor Ltv1 chaperones the assembly of the small subunit head. *J. Cell Biol.*, **217**, 4141–4154.
19. Loveland,A.B., Bah,E., Madireddy,R., Zhang,Y., Brilot,A.F., Grigorieff,N. and Korostelev,A.A. (2016) Ribosome·RelA structures reveal the mechanism of stringent response activation. *Elife*, **5**, e17029.
20. Hopes,T., Norris,K., Agapiou,M., McCarthy,C.G.P., Lewis,P.A., O'Connell,M.J., Fontana,J. and Aspden,J.L. (2021) Ribosome heterogeneity in *Drosophila melanogaster* gonads through paralog-switching. *Nucleic Acids Res.*, **50**, 2240–2257.
21. Dean,E.J., Davis,J.C., Davis,R.W. and Petrov,D.A. (2008) Pervasive and persistent redundancy among duplicated genes in yeast. *PLoS Genet.*, **4**, e1000113.
22. Rotenberg,M.O., Moritz,M. and Woolford,J.L. Jr (1988) Depletion of *Saccharomyces cerevisiae* ribosomal protein L16 causes a decrease in 60S ribosomal subunits and formation of half-mer polyribosomes. *Genes Dev.*, **2**, 160–172.
23. Gupta,V. and Warner,J.R. (2014) Ribosome-omics of the human ribosome. *RNA*, **20**, 1004–1013.
24. Segev,N. and Gerst,J.E. (2018) Specialized ribosomes and specific ribosomal protein paralogs control translation of mitochondrial proteins. *J. Cell Biol.*, **217**, 117–126.
25. Xue,S. and Barna,M. (2012) Specialized ribosomes: a new frontier in gene regulation and organismal biology. *Nat. Rev. Mol. Cell Biol.*, **13**, 355–369.
26. Burn,T.C., Connors,T.D. and Van Raay,T.J. (1996) Generation of a transcriptional map for a 700-kb region surrounding the polycystic kidney disease type 1 (PKD1) and tuberous sclerosis type 2 (TSC2) disease genes on human chromosome 16p3.3. *Genome Res.*, **6**, 525–537.
27. Van Raay,T.J., Connors,T.D., Klinger,K.W., Landes,G.M. and Burn,T.C. (1996) A novel ribosomal protein L3-like gene (RPL3L) maps to the autosomal dominant polycystic kidney disease gene region. *Genomics*, **37**, 172–176.
28. Thorolfsdottir,R.B., Sveinbjornsson,G., Sulem,P., Nielsen,J.B., Jonsson,S., Halldorsson,G.H., Melsted,P., Ivarsdottir,E.V., Davidsson,O.B., Kristjansson,R.P. *et al.* (2018) Coding variants in RPL3L and MYZAP increase risk of atrial fibrillation. *Commun. Biol.*, **1**, 68.
29. Ganapathi,M., Argyriou,L., Martínez-Azorín,F., Morlot,S., Yigit,G., Lee,T.M., Auber,B., von Gise,A., Petrey,D.S., Thiele,H. *et al.* (2020) Bi-allelic missense disease-causing variants in RPL3L associate neonatal dilated cardiomyopathy with muscle-specific ribosome biogenesis. *Hum. Genet.*, **139**, 1443–1454.
30. Al-Hassnan,Z.N., Almesned,A., Tulbah,S., Alakhfash,A., Alhadeq,F., Alruwaili,N., Alkorashy,M., Alhashem,A., Alrashdan,A., Faqeih,E. *et al.* (2020) Categorized genetic analysis in childhood-onset cardiomyopathy. *Circ. Genom. Precis. Med.*, **13**, 504–514.
31. Yang,H., Wang,H. and Jaenisch,R. (2014) Generating genetically modified mice using CRISPR/Cas-mediated genome engineering. *Nat. Protoc.*, **9**, 1956–1968.
32. Qin,W., Dion,S.L., Kutny,P.M., Zhang,Y., Cheng,A.W., Jillette,N.L., Malhotra,A., Geurts,A.M., Chen,Y.-G. and Wang,H. (2015) Efficient CRISPR/Cas9-mediated genome editing in mice by zygote electroporation of nuclease. *Genetics*, **200**, 423–430.
33. Sanz,E., Yang,L., Su,T., Morris,D.R., McKnight,G.S. and Amieux,P.S. (2009) Cell-type-specific isolation of ribosome-associated mRNA from complex tissues. *Proc. Natl Acad. Sci. USA*, **106**, 13939–13944.
34. Nishikawa,K., Yoshida,M., Kusuhara,M., Ishigami,N., Isoda,K., Miyazaki,K. and Ohsuzu,F. (2006) Left ventricular hypertrophy in mice with a cardiac-specific overexpression of interleukin-1. *Am. J. Physiol. Heart Circ. Physiol.*, **291**, H176–H83.
35. Quiros,P.M., Goyal,A., Jha,P. and Auwerx,J. (2017) Analysis of mtDNA/nDNA ratio in nice. *Curr. Protoc. Mouse Biol.*, **7**, 47–54.
36. Begik,O., Lucas,M.C., Liu,H., Ramirez,J.M., Mattick,J.S. and Novoa,E.M. (2020) Integrative analyses of the RNA modification machinery reveal tissue- and cancer-specific signatures. *Genome Biol.*, **21**, 97.
37. Mistry,J., Chuguransky,S., Williams,L., Qureshi,M., Salazar,G.A., Sonnhammer,E.L.L., Tosatto,S.C.E., Paladin,L., Raj,S., Richardson,L.J. *et al.* (2020) Pfam: the protein families database in 2021. *Nucleic Acids Res.*, **49**, D412–D419.
38. Nguyen,L.-T., Schmidt,H.A., von Haeseler,A. and Minh,B.Q. (2015) IQ-TREE: a fast and effective stochastic algorithm for estimating maximum-likelihood phylogenies. *Mol. Biol. Evol.*, **32**, 268–274.
39. Minh,B.Q., Schmidt,H., Chernomor,O., Schrempf,D., Woodhams,M., von Haeseler,A. and Lanfear,R. (2020) IQ-TREE 2: new models and efficient methods for phylogenetic inference in the genomic era. *Mol. Biol. Evol.*, **37**, 1530–1534 .
40. Cardoso-Moreira,M., Halbert,J., Valloton,D., Velten,B., Chen,C., Shao,Y., Liechti,A., Ascenção,K., Rummel,C., Ovchinnikova,S. *et al.* (2019) Gene expression across mammalian organ development. *Nature*, **571**, 505–509.
41. Sanz,E., Bean,J.C., Carey,D.P., Quintana,A. and McKnight,G.S. (2019) RiboTag: ribosomal tagging strategy to analyze cell-type-specific mRNA expression in vivo. *Curr. Protoc. Neurosci.*, **88**, e77.

42. Ackers-Johnson,M., Li,P.Y., Holmes,A.P., O'Brien,S.-M., Pavlovic,D. and Foo,R.S. (2016) A simplified, Langendorff-free method for concomitant isolation of viable cardiac myocytes and nonmyocytes from the adult mouse heart. *Circ. Res.*, **119**, 909–920.
43. Chiva,C., Olivella,R., Borràs,E., Espadas,G., Pastor,O., Solé,A. and Sabidó,E. (2018) QCloud: a cloud-based quality control system for mass spectrometry-based proteomics laboratories. *PLoS One*, **13**, e0189209.
44. Beer,L.A., Liu,P., Ky,B., Barnhart,K.T. and Speicher,D.W. (2017) Efficient quantitative comparisons of plasma proteomes using label-free analysis with MaxQuant. *Methods Mol. Biol.*, **1619**, 339–352.
45. MacLean,B., Tomazela,D.M., Shulman,N., Chambers,M., Finney,G.L., Frewen,B., Kern,R., Tabb,D.L., Liebler,D.C. and MacCoss,M.J. (2010) Skyline: an open source document editor for creating and analyzing targeted proteomics experiments. *Bioinformatics*, **26**, 966–968.
46. Vizcaíno,J.A., Csordas,A., Del-Toro,N., Dianes,J.A., Griss,J., Lavidas,I., Mayer,G., Perez-Riverol,Y., Reisinger,F., Ternent,T. *et al.* (2016) 2016 update of the PRIDE database and its related tools. *Nucleic Acids Res.*, **44**, 11033.
47. Cozzuto,L., Liu,H., Pryszcz,L.P., Pulido,T.H., Delgado-Tejedor,A., Ponomarenko,J. and Novoa,E.M. (2020) MasterOfPores: a workflow for the analysis of Oxford Nanopore direct RNA sequencing datasets. *Front. Genet.*, **11**, 211.
48. Li,H. (2018) Minimap2: pairwise alignment for nucleotide sequences. *Bioinformatics*, **34**, 3094–3100.
49. Chothani,S., Adami,E., Ouyang,J.F., Viswanathan,S., Hubner,N., Cook,S.A., Schafer,S. and Rackham,O.J.L. (2019) deltaTE: detection of translationally regulated genes by integrative analysis of Ribo-seq and RNA-seq data. *Curr. Protoc. Mol. Biol.*, **129**, e108.
50. Liu,Q., Shvarts,T., Sliz,P. and Gregory,R.I. (2020) RiboToolkit: an integrated platform for analysis and annotation of ribosome profiling data to decode mRNA translation at codon resolution. *Nucleic Acids Res.*, **48**, W218–W229.
51. Ozadam,H., Geng,M. and Cenik,C. (2020) RiboFlow, RiboR and RiboPy: an ecosystem for analyzing ribosome profiling data at read length resolution. *Bioinformatics*, **36**, 2929–2931.
52. Martin,M. (2011) Cutadapt removes adapter sequences from high-throughput sequencing reads. *EMBnet.journal*, **17**, 10–12.
53. Litvinukova,M., Lindberg,E., Maatz,H., Zhang,H., Radke,M., Gotthardt,M., Saeb-Parsy,K., Teichmann,S. and Hübner,N. (2018) Single cell and single nuclei analysis human heart tissue v1. protocols.io, https://doi.org/10.17504/protocols.io.veae3ae.
54. Wolf,F.A., Angerer,P. and Theis,F.J. (2018) SCANPY: large-scale single-cell gene expression data analysis. *Genome Biol.*, **19**, 15.
55. Bernstein,N.J., Fong,N.L., Lam,I., Roy,M.A., Hendrickson,D.G. and Kelley,D.R. (2020) Solo: doublet identification in single-cell RNA-seq via semi-supervised deep learning. *Cell Syst.*, **11**, 95–101.
56. McInnes,L., Healy,J., Saul,N. and Großberger,L. (2018) UMAP: uniform manifold approximation and projection. *J. Open Source Software*, **3**, 861.
57. Korsunsky,I., Millard,N., Fan,J., Slowikowski,K., Zhang,F., Wei,K., Baglaenko,Y., Brenner,M., Loh,P.-R. and Raychaudhuri,S. (2019) Fast, sensitive and accurate integration of single-cell data with Harmony. *Nat. Methods*, **16**, 1289–1296.
58. van Dijk,D., Sharma,R., Nainys,J., Yim,K., Kathail,P., Carr,A.J., Burdziak,C., Moon,K.R., Chaffer,C.L., Pattabiraman,D. *et al.* (2018) Recovering gene interactions from single-cell data using data diffusion. *Cell*, **174**, 716–729.
59. Simsek,D., Tiu,G.C., Flynn,R.A., Byeon,G.W., Leppek,K., Xu,A.F., Chang,H.Y. and Barna,M. (2017) The mammalian ribo-interactome reveals ribosome functional diversity and heterogeneity. *Cell*, **169**, 1051–1065.
60. Ren,Z., Yu,P., Li,D., Li,Z., Liao,Y., Wang,Y., Zhou,B. and Wang,L. (2020) Single-cell reconstruction of progression trajectory reveals intervention principles in pathological cardiac hypertrophy. *Circulation*, **141**, 1704–1719.
61. Rodríguez-Galán,O., García-Gómez,J.J., Rosado,I.V., Wei,W., Méndez-Godoy,A., Pillet,B., Alekseenko,A., Steinmetz,L.M., Pelechano,V., Kressler,D. *et al.* (2021) A functional connection between translation elongation and protein folding at the ribosome exit tunnel in *Saccharomyces cerevisiae*. *Nucleic Acids Res.*, **49**, 206–220.
62. Ravi,V., Jain,A., Ahamed,F., Fathma,N., Desingu,P.A. and Sundaresan,N.R. (2018) Systematic evaluation of the adaptability of the non-radioactive SUnSET assay to measure cardiac protein synthesis. *Sci. Rep.*, **8**, 4587.
63. Reynoso,M.A., Juntawong,P., Lancia,M., Blanco,F.A., Bailey-Serres,J. and Zanetti,M.E. (2015) Translating Ribosome Affinity Purification (TRAP) followed by RNA sequencing technology (TRAP-SEQ) for quantitative assessment of plant translatomes. *Methods Mol. Biol.*, **1284**, 185–207.
64. Moulik,M., Vatta,M., Witt,S.H., Arola,A.M., Murphy,R.T., McKenna,W.J., Boriek,A.M., Oka,K., Labeit,S., Bowles,N.E. *et al.* (2009) ANKRD1, the gene encoding cardiac ankyrin repeat protein, is a novel dilated cardiomyopathy gene. *J. Am. Coll. Cardiol.*, **54**, 325–333.
65. Crocini,C., Arimura,T., Reischmann,S., Eder,A., Braren,I., Hansen,A., Eschenhagen,T., Kimura,A. and Carrier,L. (2013) Impact of ANKRD1 mutations associated with hypertrophic cardiomyopathy on contraction parameters of engineered heart tissue. *Basic Res. Cardiol.*, **108**, 349.
66. Ingolia,N.T., Ghaemmaghami,S., Newman,J.R.S. and Weissman,J.S. (2009) Genome-wide analysis in vivo of translation with nucleotide resolution using ribosome profiling. *Science*, **324**, 218–223.
67. Lake,B.B., Codeluppi,S., Yung,Y.C., Gao,D., Chun,J., Kharchenko,P.V., Linnarsson,S. and Zhang,K. (2017) A comparative strategy for single-nucleus and single-cell transcriptomes confirms accuracy in predicted cell-type expression from nuclear RNA. *Sci. Rep.*, **7**, 6031.
68. Lacar,B., Linker,S.B., Jaeger,B.N., Krishnaswami,S.R., Barron,J.J., Kelder,M.J.E., Parylak,S.L., Paquola,A.C.M., Venepally,P., Novotny,M. *et al.* (2016) Nuclear RNA-seq of single neurons reveals molecular signatures of activation. *Nat. Commun.*, **7**, 11022.
69. Litviňuková,M., Talavera-López,C., Maatz,H., Reichart,D., Worth,C.L., Lindberg,E.L., Kanda,M., Polanski,K., Heinig,M., Lee,M. *et al.* (2020) Cells of the adult human heart. *Nature*, **588**, 466–472.
70. Bonnot,T., Gillard,M. and Nagel,D. (2019) A simple protocol for informative visualization of enriched gene ontology terms. *Bio Protoc.*, **9**, e3429 .
71. Lesnik,C., Cohen,Y., Atir-Lande,A., Schuldiner,M. and Arava,Y. (2014) OM14 is a mitochondrial receptor for cytosolic ribosomes that supports co-translational import into mitochondria. *Nat. Commun.*, **5**, 5711.
72. Gold,V.A.M., Chroscicki,P., Bragoszewski,P. and Chacinska,A. (2017) Visualization of cytosolic ribosomes on the surface of mitochondria by electron cryo-tomography. *EMBO Rep.*, **18**, 1786–1800.
73. MacKenzie,J.A. and Payne,R.M. (2004) Ribosomes specifically bind to mammalian mitochondria via protease-sensitive proteins on the outer membrane. *J. Biol. Chem.*, **279**, 9803–9810.
74. Kearse,M.G., Ireland,J.A., Prem,S.M., Chen,A.S. and Ware,V.C. (2013) RpL22e, but not RpL22e-like-PA, is SUMOylated and localizes to the nucleoplasm of Drosophila meiotic spermatocytes. *Nucleus*, **4**, 241–258.
75. Lamoliatte,F., Bonneil,E., Durette,C., Caron-Lizotte,O., Wildemann,D., Zerweck,J., Wenshuk,H. and Thibault,P. (2013) Targeted identification of SUMOylation sites in human proteins using affinity enrichment and paralog-specific reporter ions. *Mol. Cell. Proteomics*, **12**, 2536–2550.
76. Frey,N., Katus,H.A., Olson,E.N. and Hill,J.A. (2004) Hypertrophy of the heart: a new therapeutic target?*Circulation*, **109**, 1580–1589.
77. Katz,A.M. (1990) Cardiomyopathy of overload. A major determinant of prognosis in congestive heart failure. *N. Engl. J. Med.*, **322**, 100–110.
78. Frey,N. and Olson,E.N. (2003) Cardiac hypertrophy: the good, the bad, and the ugly. *Annu. Rev. Physiol.*, **65**, 45–79.
79. Wang,Y., Zhang,Y., Ding,G., May,H.I., Xu,J., Gillette,T.G., Wang,H. and Wang,Z.V. (2017) Temporal dynamics of cardiac hypertrophic growth in response to pressure overload. *Am. J. Physiol. Heart Circ. Physiol.*, **313**, H1119–H1129.
80. Ma,H., Yu,S., Liu,X., Zhang,Y., Fakadej,T., Liu,Z., Yin,C., Shen,W., Locasale,J.W., Taylor,J.M. *et al.* (2019) Lin28a regulates pathological cardiac hypertrophic growth through Pck2-mediated enhancement of anabolic synthesis. *Circulation*, **139**, 1725–1740.

81. Günthel,M., van Duijvenboden,K., de Bakker,D.E.M., Hooijkaas,I.B., Bakkers,J., Barnett,P. and Christoffels,V.M. (2021) Epigenetic state changes underlie metabolic switch in mouse post-infarction border zone cardiomyocytes. *J. Cardiovasc. Dev. Dis.*, **8**, 134.
82. Liu,W., Shen,J., Li,Y., Wu,J., Luo,X., Yu,Y., Zhang,Y., Gu,L., Zhang,X., Jiang,C. *et al.* (2021) Pyroptosis inhibition improves the symptom of acute myocardial infarction. *Cell Death. Dis.*, **12**, 852.
83. Filipovska,A. and Rackham,O. (2013) Specialization from synthesis: how ribosome diversity can customize protein function. *FEBS Lett.*, **587**, 1189–1197.
84. Ghulam,M.M., Catala,M. and Abou Elela,S. (2020) Differential expression of duplicated ribosomal protein genes modifies ribosome composition in response to stress. *Nucleic Acids Res.*, **48**, 1954–1968.
85. Petibon,C., Malik Ghulam,M., Catala,M. and Abou Elela,S. (2021) Regulation of ribosomal protein genes: an ordered anarchy. *Wiley Interdiscip. Rev. RNA*, **12**, e1632.
86. Ferretti,M.B., Ghalei,H., Ward,E.A., Potts,E.L. and Karbstein,K. (2017) Rps26 directs mRNA-specific translation by recognition of Kozak sequence elements. *Nat. Struct. Mol. Biol.*, **24**, 700–707.
87. Locati,M.D., Pagano,J.F.B., Girard,G., Ensink,W.A., van Olst,M., van Leeuwen,S., Nehrdich,U., Spaink,H.P., Rauwerda,H., Jonker,M.J. *et al.* (2017) Expression of distinct maternal and somatic 5.8S, 18S, and 28S rRNA types during zebrafish development. *RNA*, **23**, 1188–1199.
88. Rogers,M.J., Gutell,R.R., Damberger,S.H., Li,J., McConkey,G.A., Waters,A.P. and McCutchan,T.F. (1996) Structural features of the large subunit rRNA expressed in *Plasmodium falciparum* sporozoites that distinguish it from the asexually expressed subunit rRNA. *RNA*, **2**, 134–145.
89. Vembar,S.S., Droll,D. and Scherf,A. (2016) Translational regulation in blood stages of the malaria parasite *Plasmodium* spp.: systems-wide studies pave the way. *Wiley Interdiscip. Rev. RNA*, **7**, 772–792.
90. Wong,Q.W.-L., Li,J., Ng,S.R., Lim,S.G., Yang,H. and Vardy,L.A. (2014) RPL39L is an example of a recently evolved ribosomal protein paralog that shows highly specific tissue expression patterns and is upregulated in ESCs and HCC tumors. *RNA Biol*, **11**, 33–41.
91. Jiang,L., Li,T., Zhang,X., Zhang,B., Yu,C., Li,Y., Fan,S., Jiang,X., Khan,T., Hao,Q. *et al.* (2017) RPL10L is required for male meiotic division by compensating for RPL10 during meiotic sex chromosome inactivation in mice. *Curr. Biol.*, **27**, 1498–1505.
92. Narla,A. and Ebert,B.L. (2010) Ribosomopathies: human disorders of ribosome dysfunction. *Blood*, **115**, 3196–3205.
93. O'Leary,M.N., Schreiber,K.H., Zhang,Y., Duc,A.-C.E., Rao,S., Hale,J.S., Academia,E.C., Shah,S.R., Morton,J.F., Holstein,C.A. *et al.* (2013) The ribosomal protein Rpl22 controls ribosome composition by directly repressing expression of its own paralog, Rpl22l1. *PLoS Genet.*, **9**, e1003708.
94. Xiao,Z., Zou,Q., Liu,Y. and Yang,X. (2016) Genome-wide assessment of differential translations with ribosome profiling data. *Nat. Commun.*, **7**, 11194.
95. Pagliara,V., Saide,A., Mitidieri,E., d'Emmanuele di Villa Bianca,R., Sorrentino,R., Russo,G. and Russo,A. (2016) 5-FU targets rpL3 to induce mitochondrial apoptosis via cystathionine-β-synthase in colon cancer cells lacking p53. *Oncotarget*, **7**, 50333–50348.
96. Kao,B.R., Malerba,A., Lu-Nguyen,N.B., Harish,P., McCarthy,J.J., Dickson,G. and Popplewell,L.J. (2021) Knockdown of muscle-specific ribosomal protein L3-like enhances muscle function in healthy and dystrophic mice. *Nucleic Acid Ther.*, **31**, 457–464.
97. Zhou,X., Lowdon,R.F., Li,D., Lawson,H.A., Madden,P.A.F., Costello,J.F. and Wang,T. (2013) Exploring long-range genome interactions using the WashU Epigenome Browser. *Nat. Methods*, **10**, 375–376.
98. Gabunilas,J. and Chanfreau,G. (2016) Splicing-mediated autoregulation modulates Rpl22p expression in *Saccharomyces cerevisiae*. *PLoS Genet.*, **12**, e1005999.
99. Meskauskas,A., Petrov,A.N. and Dinman,J.D. (2005) Identification of functionally important amino acids of ribosomal protein L3 by saturation mutagenesis. *Mol. Cell. Biol.*, **25**, 10863–10874.
100. Al-Hadid,Q., Roy,K., Chanfreau,G. and Clarke,S.G. (2016) Methylation of yeast ribosomal protein Rpl3 promotes translational elongation fidelity. *RNA*, **22**, 489–498.
101. Yokoyama,T., Machida,K., Iwasaki,W., Shigeta,T., Nishimoto,M., Takahashi,M., Sakamoto,A., Yonemochi,M., Harada,Y., Shigematsu,H. *et al.* (2019) HCV IRES captures an actively translating 80S ribosome. *Mol. Cell*, **74**, 1205–1214.
102. Pieper,U., Webb,B.M., Dong,G.Q., Schneidman-Duhovny,D., Fan,H., Kim,S.J., Khuri,N., Spill,Y.G., Weinkam,P., Hammel,M. *et al.* (2014) ModBase, a database of annotated comparative protein structure models and associated resources. *Nucleic Acids Res.*, **42**, D336–D346.